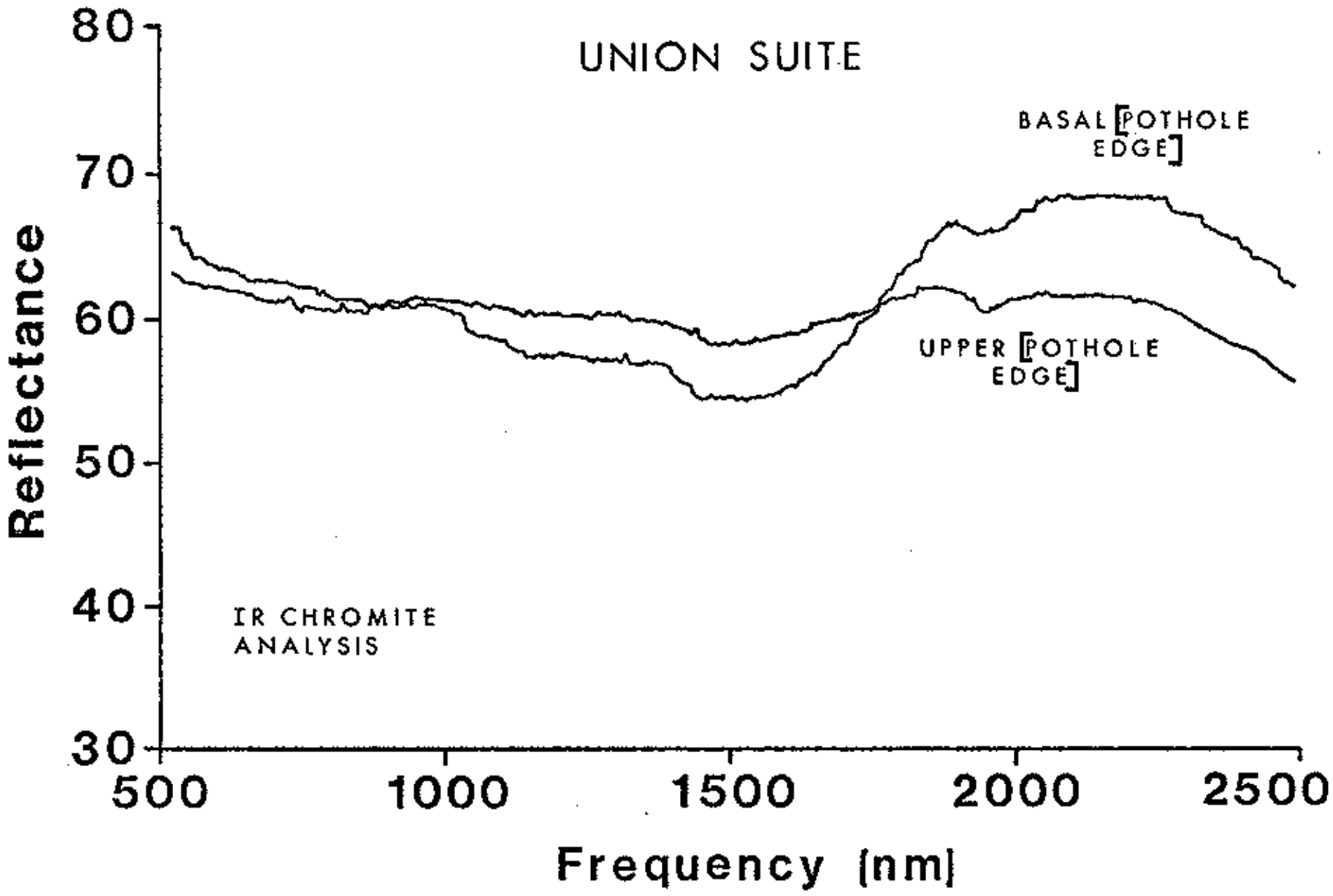
UNION SUITE
BASAL [POTHOLE EDGE]
UPPER [POTHOLE EDGE]
IR CHROMITE ANALYSIS
Reflectance
80
70
60
50
40
30
500
1000
1500
2000
2500
Frequency (nm)

fO_2 values (carbon content is not available) while, as at Rustenburg, these parameters as a class negatively correlate with Δ% reflectance and R_2O_3 content.

TABLE II

Synthesis of Data on Potholes Chromites

Rustenburg Samples

Parameters	Normal Merensky	Pothole Edge	Pothole Bottom
Fe^{+3} wt. %*1	11.47	9.59	2.90
Inorganic Carbon (ppm)	131	256	1,835
Δ % Reflectance*2	6	16	30
R_2O_3 as $(Cr_2O_3 + Al_2O_3)$*3	50.76	55.26	61.54
- log fO_2 at 1150C°	12.9	13.2	13.4

Impala Samples

Fe^{+3} wt. %*1	15.84[4]	N/A	12.81
Inorganic Carbon (ppm)	N/A	N/A	N/A
Δ % Reflectance*2	16	N/A	4
R_2O_3 as $(Cr_2O_3 + Al_2O_3)$*3	50.16[4]	N/A	52.06
- log fO_2 at 1150C°	12.1	N/A	13.9

Union Samples

	Upper Pothole Edge	Basal Pothole Edge
Fe^{+3} wt. %*1	14.21	12.79
Inorganic Carbon (ppm)	N/A	N/A
Δ % Reflectance*2	3	15
R_2O_3 as $(Cr_2O_3 + Al_2O_3)$*3	46.86	53.01
- log fO_2 at 1150C°	13.3	13.5

Table II (Continued)

*1 Stoichiometric and normative assumption involved on electronprobe analyses.

*2 The derived quantity Δ% reflectance (1500-2200 nm) is a geometric descriptive factor which gives numeric comparison among the graphic spectra (figures 52-54).

*3 High values here correlate with more normal spinel lattice coordination. As discussed by Ulmer (1981) coordination changes may not be linear with solid solution composition changes. Electron microprobe analyses data are used to derive these R_2O_3 values.

*4 Values renormalized to 100% as iron, chromium, aluminum, and magnesium totals equalled only 92.3% whereas similar totals for pothole bottom analyses equaled 99.8% without normalization.

DISCUSSION

Summary of Parameters

Within this study four major parameters indicate that potholes have a chemistry which differs from the Normal Merensky Reef. These parameters are: intrinsic oxygen fugacity analyses, carbon concentration analyses, electronprobe determination of major elements in addition to total Fe (as FeO)/(MgO + total Fe (as FeO)) ratios in chromite spinels, and reflectance near-infrared spectroscopic analyses of Fe distribution in chromite spinels. These parameters, for convenience of discussion, are superimposed upon sketches of the Rustenburg pothole (Figure 49), Impala Pothole (Figure 50), and Union pothole (Figure 51).

Rustenburg Pothole

A cross-comparison of three parameters from the Rustenburg suite analyses are provided in Figure 49. Intrinsic oxygen fugacity data demonstrate a lateral "zonation of reduction": the pothole bottom chromite and pegmatoidal pyroxenite are more reduced than the pothole edge chromite and pegmatoidal pyroxenite which in turn are more reduced than the adjacent Normal Merensky Reef chromite and pegmatoidal pyroxenite. The total Fe (as FeO)/(MgO + total Fe (as FeO)) ratios show a gradient or "zonation of reduction" whose pattern parallels that of the IOF analyses. That is, the pothole bottom chromite has a smaller ratio than the pothole edge chromite which in turn has an even smaller ratio than the Normal

Figure 49: Schematic of the Rustenburg pothole with superpositioning of the oxygen, total Fe (as FeO)/(MgO + total Fe (as FeO)) ratios, and carbon parameters. The asterisks at each sample locality are as discussed in figure 10. The data at each asterisk is listed from top to bottom as O, total Fe/Mg ratios, and C. It is important to note that total Fe, Mg, O, and C lateral gradients are not linear. That is, the range of data in all parameters is much greater between the pothole bottom and pothole edge than between the Normal Merensky Reef and pothole edge. Also, a vertical fO_2 gradient exists between An footwall and basal chromites. N/A means that not enough chromite was available for analyses.

RUSTENBURG POTHOLE
(not to scale)

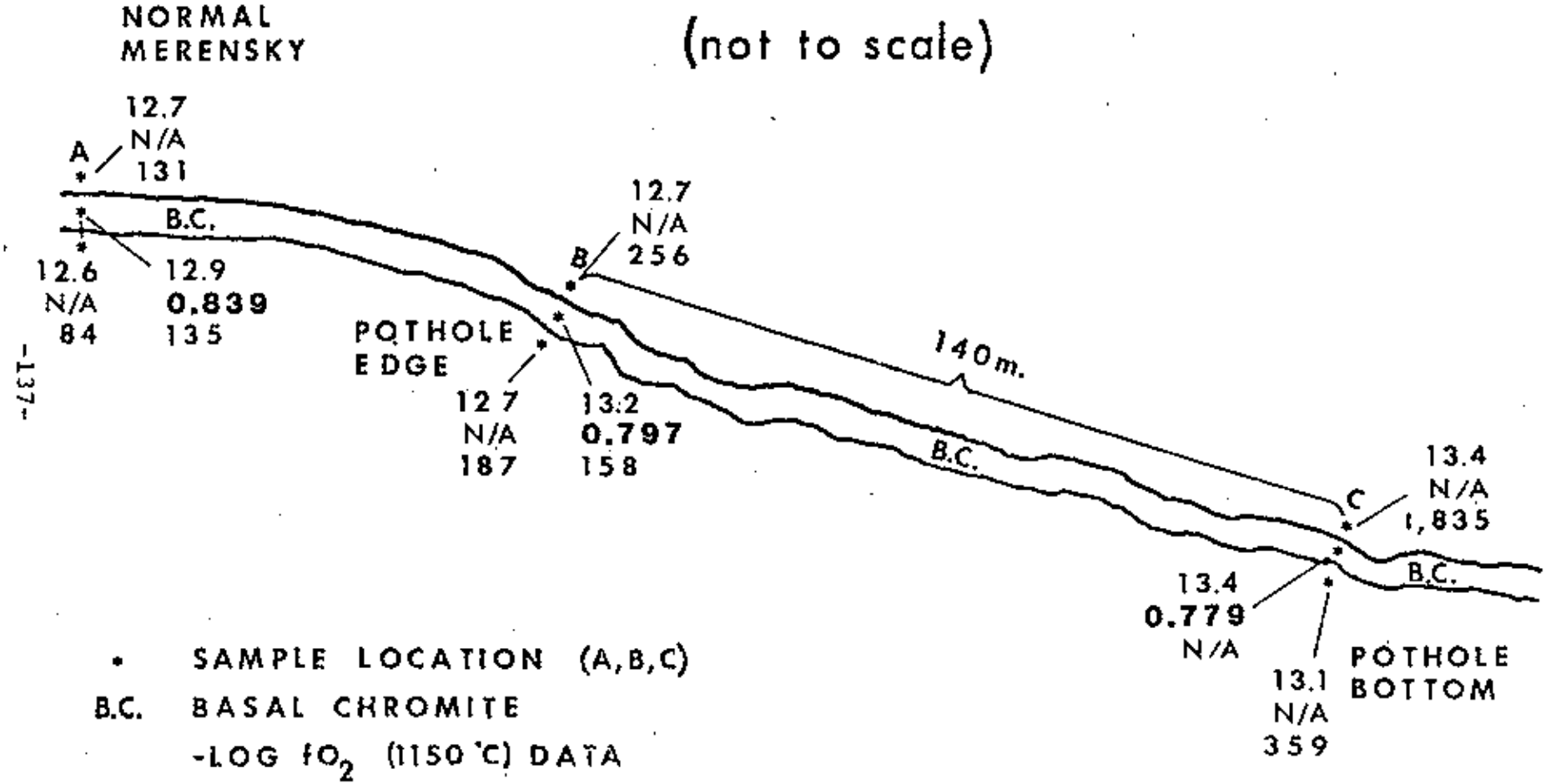

• SAMPLE LOCATION (A,B,C)

B.C. BASAL CHROMITE

-LOG fO_2 (1150 °C) DATA

TOTAL Fe(as FeO) / (MgO + TOTAL Fe(as FeO))

CARBON CONCENTRATION

ppm (wt. %)

Merensky Reef chromite. The concentration of inorganic carbon also parallels the IOF gradient in that the pothole bottom has the greatest concentration whereas the pothole edge and Normal Merensky Reef have much smaller values, implying that the greatest buffering and reduction capacity should have occurred in the pothole bottom. Additionally, a small but significant vertical gradient exists between the footwall and Normal Merensky Reef in carbon and oxygen. Carbon concentration is lower in the footwall layer than in the Normal Merensky Reef rocks while the fO_2 of the footwall is less reduced than the fO_2 of the Normal Merensky Reef rocks.

The plutonic fumarole hypothesis states that carbonaceous fluids evolving from a plutonic fumarole could crack (e.g., $CH_4 = C + 2H_2$ or $2CO = C + CO_2$) and could give rise to inorganic carbon. Evidence of "cracking" exists in that lumps of carbon sometimes as large as a desk are found in the lower extremities of potholes (pers. comm., Kennedy, 1981). Since the Rustenburg data show an order of magnitude difference between pothole bottom and Normal Merensky Reef in terms of carbon, it appears that at least this pothole bottom was a localized region of input for carbonaceous fluids. That the pothole edge and Normal Merensky Reef still contain carbon, but are both depleted in carbon relative to the pothole bottom, suggests that the fluid concentration was highest in the pothole and less concentrated out upon the Merensky event-horizon, i.e., the pothole was a conduit or plutonic fumarole.

Von Gruenewaldt (1979) does not discuss the idea of graphite-enrichment in his hypothesis. However, the distribution of carbon in the Rustenburg pothole could theoretically be accounted for by the streaming of interstitial footwall liquids, given the assumption that graphite or carbonacaeous fluids are intrinsic to these interstitial liquids. Therefore, this author feels that the observed distribution of carbon neither refutes or supports Von Greunewaldt's hypothesis as it is presently stated.

Carbonaceous fluids would partially or completely buffer the magmatic fO_2 in the vicinity of the Rustenburg pothole. As stated earlier, the carbonaceous fluids would become less concentrated as they disseminated from the injection sites of plutonic fumaroles, implying that an fO_2 gradient would develop in the magma in a parallel fashion to the carbon gradient. The oxygen and carbon gradients shown in figure 55 clearly suggest such a correlation between these paramenter, which suggests carbon was an important and controlling variable.

Near-infrared analyses (figure 46) show an increase of total iron from the pothole bottom to the Normal Merensky Reef. The pattern at 2200 nm and at 1500 nm clearly indicates that the Fe^{+3} component of total Fe, as suggested by electronprobe data, is less abundant in the pothole bottom than in the pothole edge and Normal Merensky Reef. This gradient of Fe^{+3} reflects the changing local fO_2 in the

vicinity of the pothole in that the infrared pattern also parallels that of the IOF analyses (see table II).

Electron Microprobe data indicates that gradients of Mg, Cr, Al, and total Fe exist along stratigraphically equivalent basal chromite horizons (see table I). These gradients may reflect the aforementioned fO_2 gradient in that: 1) low fO_2 (10^{-13} or greater) in the pothole bottom allowed rapid development of chromite-rich spinels, i.e., electronprobe Cr values are highest in pothole bottom chromites, 2) low Fe^{+3} in the pothole bottom chromites reflect the initial rapid inclusion of $FeAl_2O_4$ and $FeCr_2O_4$ end-members in said chromites, i.e., electronprobe data show high total Al^{+3} and low total Fe in pothole bottom chromites, 3) Mg^{+2} (which substitutes for Fe^{+2}) would not be favored by the low fO_2 in the pothole bottom, i.e., electronprobe Mg values are low in pothole bottom chromites. The major element changes in these spinels are all in keeping with the general change in spinel solid solution chemistry as a function of fO_2, e.g., Ulmer (1970).

In summary, the Rustenburg data is strongly supportive of the plutonic fumarole hypothesis in that: 1) carbonaceous buffering of fO_2 is indicated by reciprocal gradients in C and O, 2) total Fe (as FeO)/(MgO + total Fe (as FeO)) ratios in basal chromite spinels parallel the measured fO_2 gradient, 3) near-infrared determination of Fe^{+3} distribution in chromite spinels also parallel said fO_2 gradient, 4) Mg, Cr, Al, and total Fe gradients in basal chromites parallel the

measured fO_2 gradient, and 5) all parameters indicate lateral changes along stratigraphically equivalent horizons.

A vertical gradient of oxygen and carbon exist between the footwall and basal Merensky Reef chromite. The vertical gradient of fO_2 is explained by the plutonic fumarole hypothesis in that the IOF of footwall rocks should not be as affected by the injection of carbonaceous fluids, as would be the later precipitating Merensky Reef. That is, the intrinsic oxygen fugacity of footwall anorthosites, being a crystalline mush prior to the injection of carbonaceous fluids, should not have achieved as reduced an equilibrium with the fO_2 as would the Merensky Reef magma. Therefore, the measured fO_2 of the anorthositic footwall reflects that of the magma prior to the injection of carbonaceous fluids. Also, chromite and anorthosite was not in equilibrium prior to the Merensky Reef event as the footwall immediately below the Merensky Reef is chromite free. Thus, the measured differences in fO_2 at 1150°C are real since no equilibrium between footwall anorthosite and basal Merensky chromite existed. It is important to note that the Rustenburg suite shows a lateral fO_2 gradient within the footwall unit. The author feels this measured gradient is due to either: 1) small inclusions of chromite within the still mushy An footwall which could have lowered the fO_2 of the analyzed An, or 2) the pertubation of the intrinsic fO_2 of the interstitial liquid in the footwall anorthositic mush by strong reducing fluids in the vicinity of the pothole. Either of these two possibilities are

probably equally possible because the author selected An for analyses only a few tens of millimeters below the basal chromitite layer.

The vertical gradient of carbon is also explained by the plutonic fumarole hypothesis in that carbonaceous fluids would have difficulty dissemination laterally into already mushy anorthositic footwall rocks. Thus, little if any, "cracking" of said fluids would occur within the footwall to produce a distinct lateral carbon gradient. The slightly higher value of carbon concentration in the pothole bottom anorthositic footwall, relative to the pothole edge and Normal Merensky Reef footwall, is attributed to the higher inferred volatile fluid concentration in the pothole with consequent "cracking" at and along the top of the footwall.

Impala Pothole

Figure 50 cross-compares lateral gradients in oxygen and total Fe(as FeO)/(MgO + total Fe(as FeO)) ratios. IOF data from the basal chromite show a lateral "zonation of reduction" in that pothole bottom chromite is significantly more reduced than Normal Merensky Reef chromite while total Fe (as FeO)/(MgO + total Fe (as FeO)) ratios show a lateral "zonation of reduction" which correlates with the IOF gradient. Table 1 shows that total Fe, Mg, Al, and Cr distribution in basal chromite spinels correlates with the IOF gradient while near-infrared analyses show a similar correlation between IOF and Fe^{+3} distribution. Additionally,

Figure 50: Schematic of the Impala pothole with superpositioning of the oxygen and total Fe (as FeO)/(MgO + total Fe (as FeO)) ratio parameters. The asterisks at each sample locality are as discussed in figure 20. The data at each asterisk is listed from top to bottom as oxygen and total Fe (as FeO)/(MgO + total Fe (as FeO)) ratios. Note the lateral gradients of oxygen and total Fe (as FeO)/(MgO + total Fe (as FeO)) ratios and the subtle fO_2 gradient between An footwall and the basal chromite.

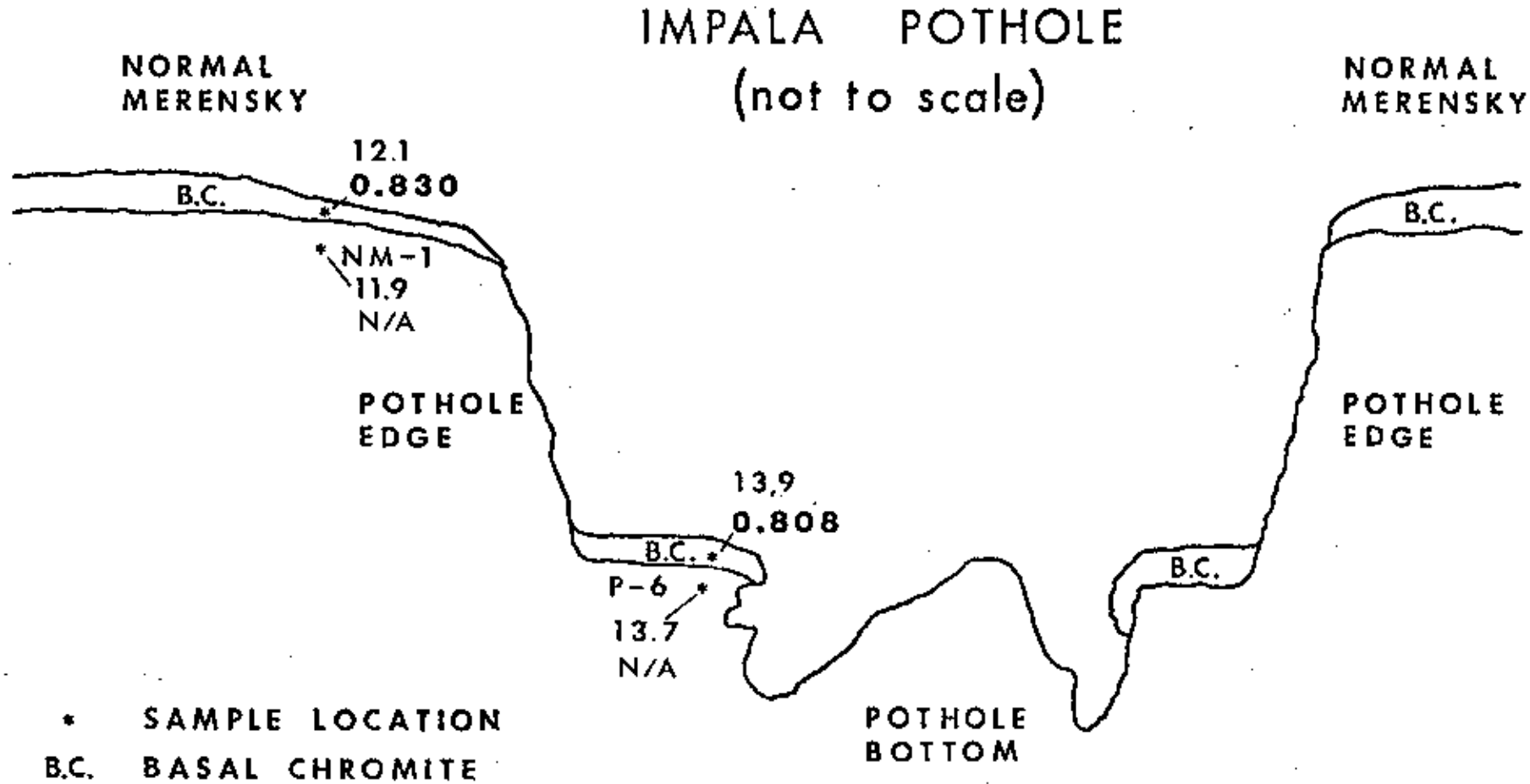
IMPALA POTHOLE
(not to scale)
NORMAL MERENSKY
NORMAL MERENSKY
12.1
0.830
B.C.
*NM-1
11.9
N/A
POTHOLE EDGE
POTHOLE EDGE
B.C.
13.9
0.808
B.C.
P-6
13.7
N/A
B.C.
POTHOLE BOTTOM
* SAMPLE LOCATION
B.C. BASAL CHROMITE
-LOG fO_2 (1150 °C) DATA
TOTAL Fe(as FeO) / (MgO + TOTAL Fe(as FeO))

a subtle vertical gradient exists between the footwall anorthosite and basal chromite as shown by the fO_2 data.

The plutonic fumarole hypothesis readily accounts for these lateral and vertical gradients. The reader is referred to the arguments listed above in the Rustenburg suite discussion for the establishment of these gradients; the same ideas are again applicable to these Impala pothole data.

Union Pothole

The Union pothole (Figure 51) samples are restricted to the pothole edge. Therefore, no lateral gradient could be deduced. However, non-stratigraphically equivalent vertical gradients are examined between the basal and upper chromites. A small fO_2 gradient exists between the footwall and basal chromite, while an equally small fO_2 gradient exists between the basal and upper chromites.

The plutonic fumarole hypothesis may account for these subtle vertical gradients. The argument for said gradient between the footwall and basal chromite in the Union pothole is identical to the arguement presented above in the Rustenburg pothole discussion. The existence of a subtle fO_2 gradient between the upper and basal chromite may reflect decreasing concentrations of carbonaceous fluids during the emplacement of the upper Merensky Reef chromite. The author postulates that the "fin" in this pothole was an active plutonic fumarole during Merensky Reef time. The termination of carbonaceous fluid discharge from the fumarole may or may not have ceased before the Merensky Reef event came to a

Figure 51: Schematic of the Union pothole with superpositioning of the oxygen and total Fe (as FeO)/(MgO + total Fe (as FeO)) ratio parameters. The asterisks at each sample locality are as discussed in figure 16. The data at each asterisk is listed from top to bottom as oxygen and total Fe (as FeO)/(MgO + total Fe (as FeO)) ratios. Note the vertical gradients in oxygen and iron between the upper and basal chromite and the subtle fO_2 gradient between An footwall and basal chromite.

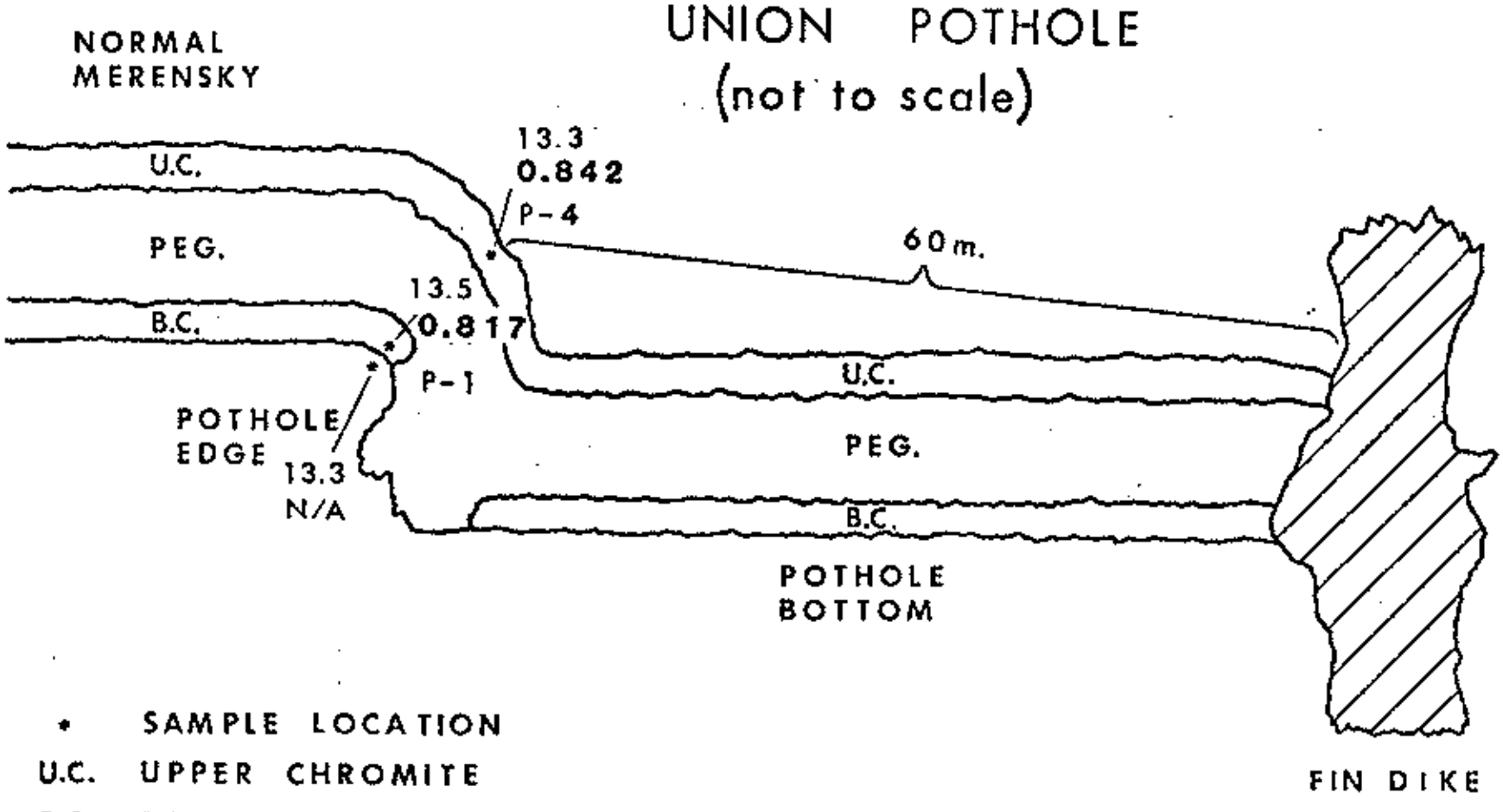

* SAMPLE LOCATION

U.C. UPPER CHROMITE

B.C. BASAL CHROMITE

PEG. PEGMATOID

$-\log fO_2$ (1150 °C) DATA

TOTAL Fe(as FeO) / (MgO - TOTAL Fe(as FeO))

close. In either case, the upper Merensky Reef chromites would reflect the returning of the Bushveld magma fO_2 to more "normal" conditions as volatile fluid concentrations became lower at the upper Merensky time, i.e., textures become fine grained again after the Merensky Reef event.

The measured change in fO_2 is substantiated by electronprobe data which show well defined gradients in total Fe and Al (Figure 51 and Table I). Additionally, near-infrared analyses (Figure 48) show a positive correlation between IOF and Fe^{+3} distribution.

Analyses of the Union pothole gradients show that the plutonic fumarole hypothesis need not be restricted to time-stratigraphic units. The fin in this Union pothole contains cognate fragments of the lower Merensky units but not of the hanging wall units. This would seem to imply pene-contemporaneous origin of the fin-dike with Merensky time. Furthermore, the fin-dike pinches out quickly in the hanging wall and footwall at this pothole. It is this fin-dike which, in fact, "started" the plutonic fumarole hypothesis (Ulmer's field notes, (1974). Hence, the vertical gradients are in fact totally expected if the plutonic fumarole hypothesis is correct. The fluid pulse injection may not have been "instantaneous", but the magma in subsequent cumulate horizons may have returned to more normal conditions.

Hypotheses Cross-Comparison

As discussed in the introduction, the validity of the plutonic fumarole hypothesis resides in the confirmation of gradients or "zonations of reduction" from potholes to the adjacent Normal Merensky Reef. Lateral gradients have been confirmed in the Rustenburg and Impala pothole while vertical gradients between the footwall and basal chromites have been confirmed in all analyzed potholes in addition to the vertical gradients between the basal and upper chromite of the Union pothole. At this time, the plutonic fumarole hypothesis is in fact the only viable hypothesis which explains the measured concentration gradients at these three studied potholes.

The development of potholes by hypotheses which invoke scouring phenomena is clearly refuted for the three potholes studied herein. That is, potholes which were formed by convective scouring or abrasion and "back-filled" with Normal Merensky Reef should not exhibit chemistries as different from the Normal Merensky Reef as have been observed in this study.

The formation of potholes by streaming intrinsic silicate footwall liquids is physically possible but is doubtful as the mechanism of pothole development on the Merensky Reef: Von Gruenewaldt's hypothesis states that potholes formed by silicate liquid streaming through an already formed but still mushy Merensky Reef. Unless somehow enriched in carbonaceous fluids, streaming interstitial footwall liquids probably

would not give rise to the gradients found in this study. In the plutonic fumarole hypothesis these gradients would be established as the Merensky Reef was precipitating, i.e., either metasomatic fluids from the sedimentary footwall under the entire Bushveld Complex, or juvenile volatiles from the mantle could provide the carbonaceous enrichments. Consequently, by virtue of the existence of these pothole gradients, the author feels that while Von Gruenewaldt's hypothesis may have merit, it can not account for some of these new data.

Merensky Reef Development as a Response to Plutonic Fumaroles[3]

The plutonic fumarole hypothesis envisions the source of carbonaceous and/or sulfurous fluids as being either mantle-derived or baked out of sedimentary units which floor the Bushveld Igneous Complex. Research by Vermaak (1970) on the Western Bushveld indicate that quartzites, carbonates, and shales constitute these sedimentary units and that metamorphic aureoles extend for thousands of meters into said units. Thus, it is entirely feasible that these sediments released enough metasomatic fluids to reach overburden pressure, releasing said fluids into the Bushveld chamber.

---

3 The author acknowledges that this term, plutonic fumarole, is a new juxtaposition of two standard words and therefore defines the new term as a volatile-rich emanation or conduit in a mushy plutonic environment. The juxtaposition furthermore is credited to Dr. R. Flynn (pers. comm; also cf. Flynn et al.,1978).

The sequence of events by which these volatile fluids may have reached the Bushveld magma are depicted in Figure 5.

Various analyses of the Critical Zone (Merensky Reef footwall) are germain to the development of the plutonic fumarole model of Merensky Reef emplacement. Elliott et al (1982) provide analyses of chromites for 677 vertical meters below the Merensky Reef (Figure 52). The analyses show that Critical Zone chromites maintained a log fO_2 of approximately $10^{-13.7\pm 0.7}$ at 1150°C. As they explain, this low value of log fO_2 suggests both the presence of carbon and that the magma was on the verge of sulfide immiscibility prior to Merensky Reef emplacement, i.e., the fO_2 need only have lowered a few tenths of a log unit to produce an immiscible sulfide phase. Additionally, Liebenburg (1970) has shown that the sulfide content of the Merensky Reef footwall is between one and two orders of magnitude less than the sulfide content of the Merensky Reef, implying that the Merensky Reef was an event corresponding to the development of a major sulfide immiscibility. Finally, Cameron (1982) in his analyses of Critical Zone (Merensky Reef footwall) rocks demonstrates that no major injection of new magma occurred from the L-horizon to the base of the Merensky Reef. Combining the above cited studies we have a general picture of Merensky Reef footwall rocks as undergoing a normal Bowen differentiation <u>in situ</u> on the verge of sulfide immiscibility from the L-horizon to the base of the Merensky Reef.

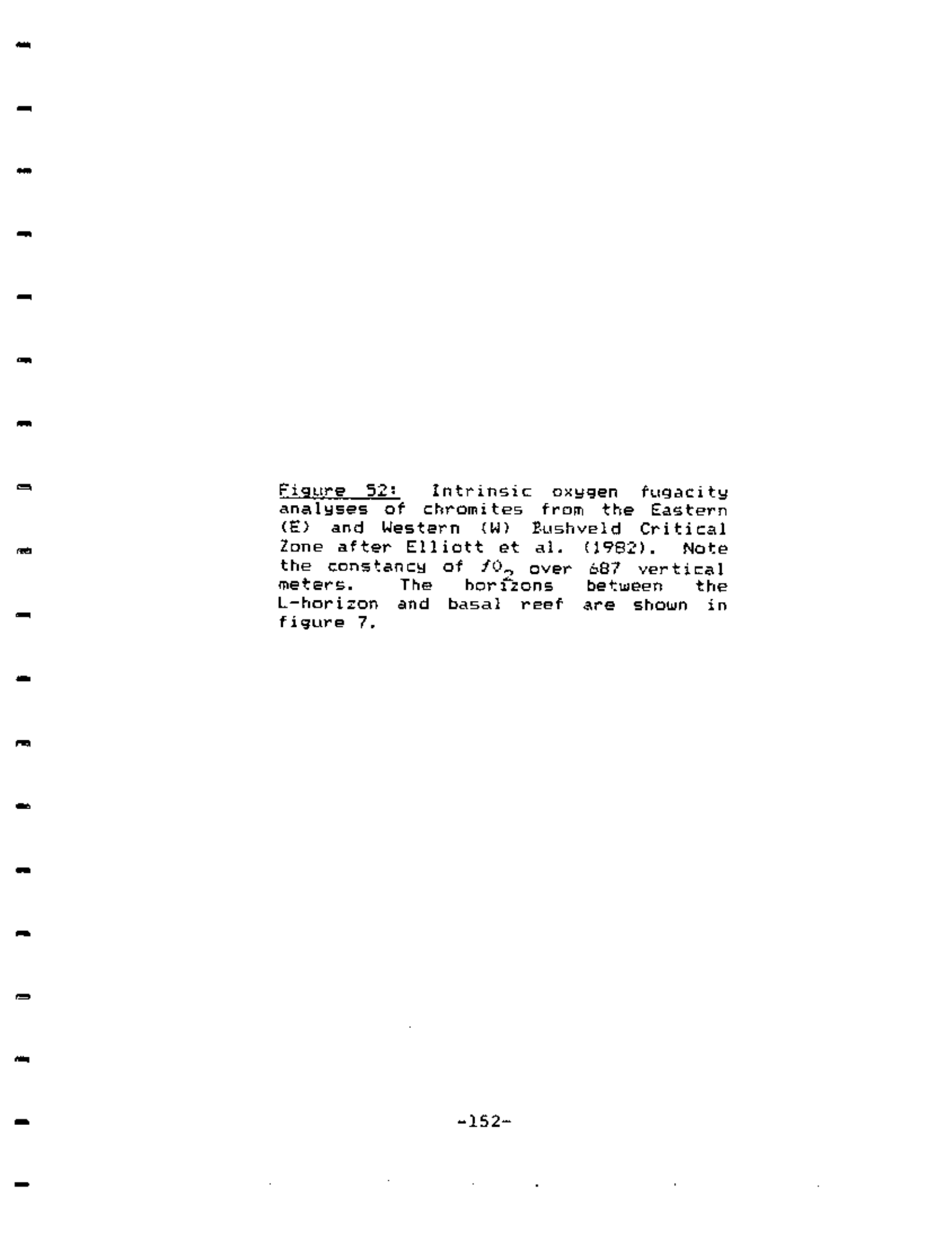

Figure 52: Intrinsic oxygen fugacity analyses of chromites from the Eastern (E) and Western (W) Bushveld Critical Zone after Elliott et al. (1982). Note the constancy of fO_2 over 687 vertical meters. The horizons between the L-horizon and basal reef are shown in figure 7.

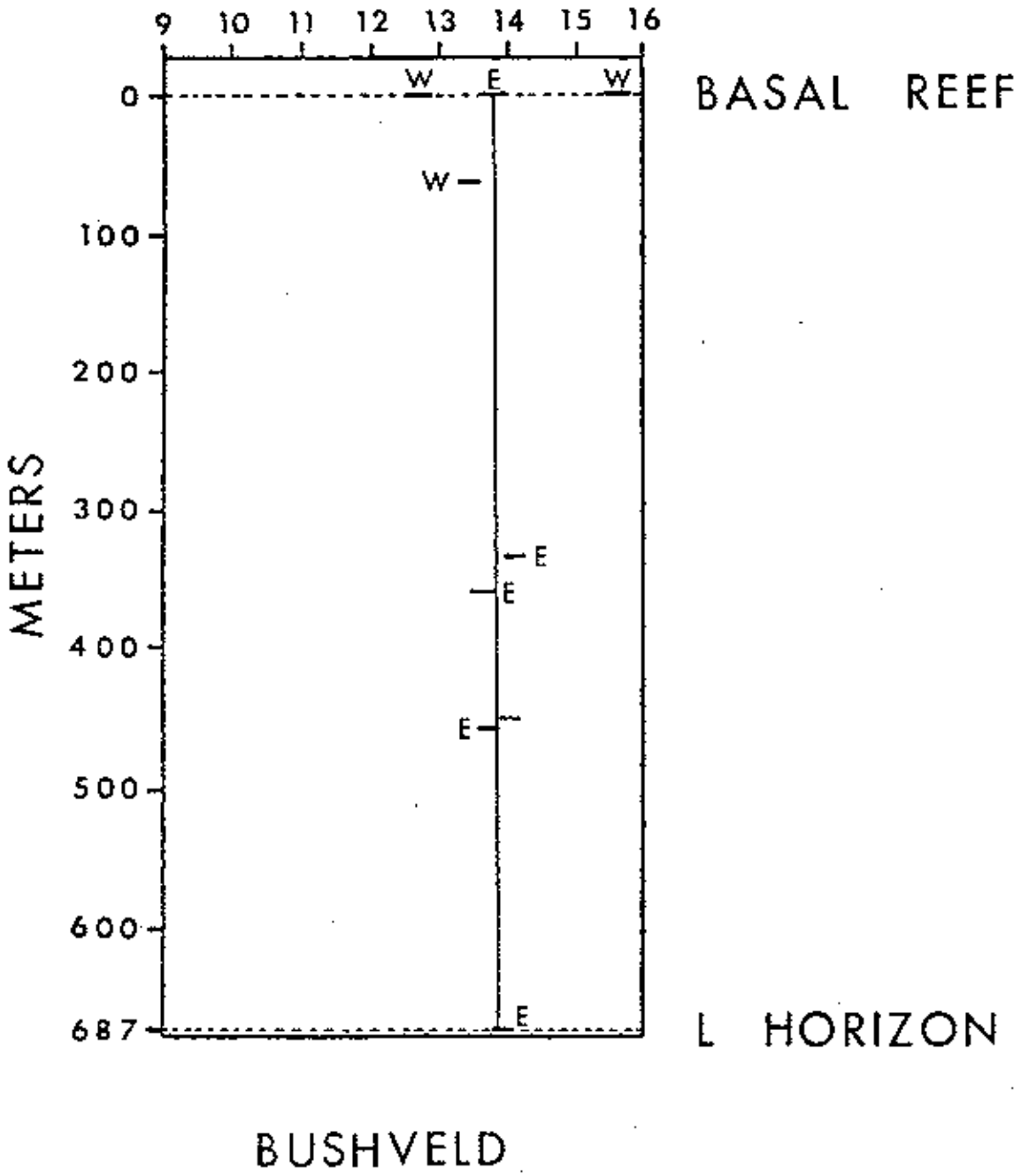

(ELLIOT et al., 1982)

Given the above conditions in the footwall data, the author cites Haughton et al. (1974) in order to explain the development of immiscible sulfide liquids during Merensky Reef emplacement. A diagram of particular importance from their paper, recreated in Figure 53, shows that a decrease of fO_2 in a magma with a fixed fS_2 will produce an immiscible sulfide liquid. They further comment that assimilation of carbonaceous material would easily lower the fO_2 of said magma. Additionally, Haughton relates that direct assimilation of H_2S or SO_2 by a magma would increase the fS_2, thereby producing an immiscible sulfide liquid as shown in Figure 53. The plutonic fumarole hypothesis meets the prerequisites necessary for sulfide immiscibility in that the fO_2 may be lowered by the injection of carbonaceous gases or the fS_2 may be increased by the injection of sulfurous gases. Additionally, the plutonic fumarole hypothesis does not rule out the simultaneous injection of both carbonaceous and sulfurous fluids, thereby operating in tandem to lower the fO_2 and increase fS_2. This possibility would produce copious amounts of immiscible sulfide liquid. However, some potholes do not show an increase in sulfide content as compared to the Normal Merensky (Kinloch, pers. comm.).

Research by Buchanan and Nolan (1979) also support the notion that the Merensky Reef sulfides formed in response to a pertubation in fO_2, fS_2, or both. Their research on basaltic melts at one atmosphere pressure demonstrated that immiscible sulfides develop at 1200°C when the ratio of

Figure 53: Relation between fO_2, fS_2, FeO, and S contents of basaltic magma at 1200°C after Haughton et al. (1974). The sulfide saturation surface defines the sulfur content of a magma in equilibrium with a sulfide melt. Tie lines connecting coexisting melts are parallel to the axis on which the sulfur content is plotted (vertical). Shaded planes in the silicate melt volume are contours of constant FeO content of the magma. The circles, T, S, Y, W, represent silicate melts on the sulfide saturation surface (shaded). These silicate melts coexist with sulfide melts T', S', Y', W'. Note that at constant fS_2 and wt. % S in a silicate melt that a decrease of fO_2 will cause development of an immiscible sulfide liquid (see text for other pathways that will produce sulfides).

SOLUBILITY OF SULFUR IN MAFIC MAGMAS

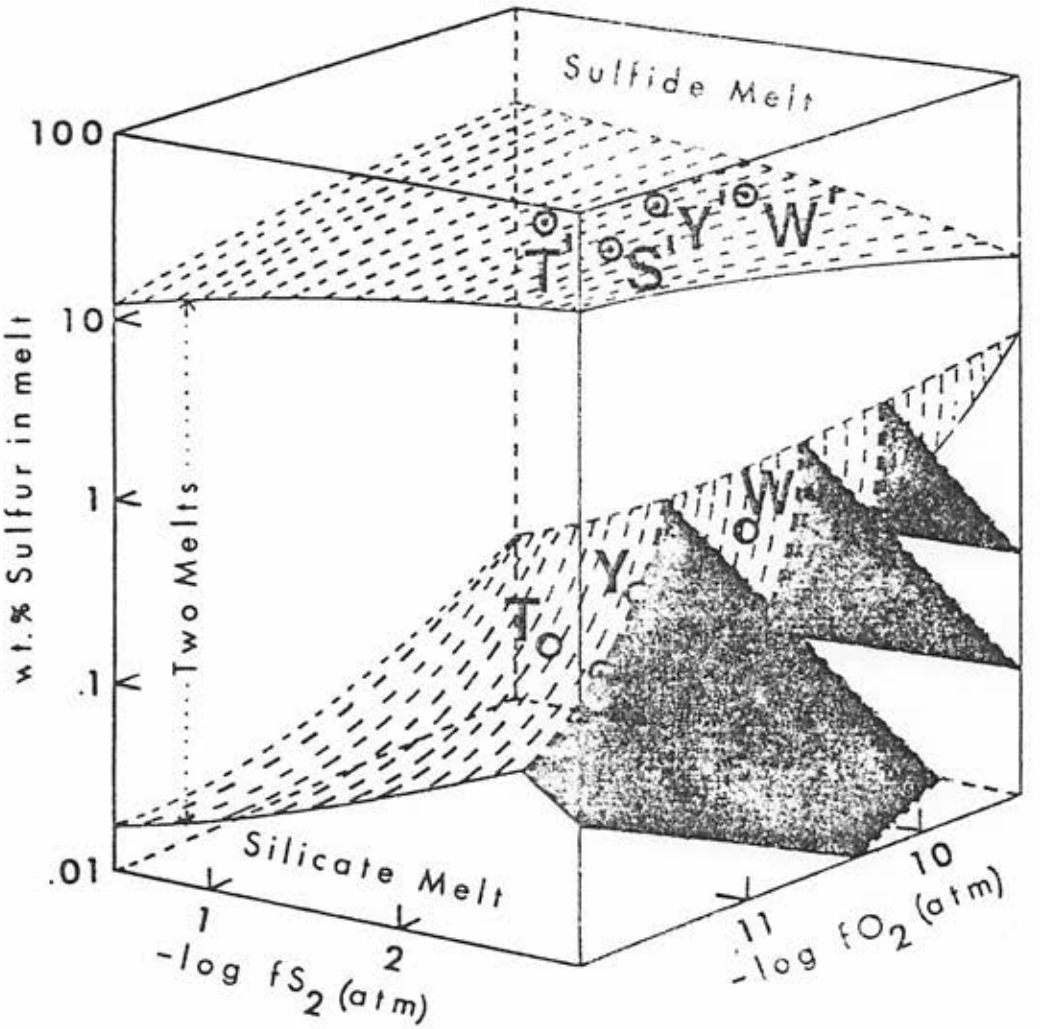

(Haughton et al., 1974)

fS_2/fO_2 exceeds 10^8 atm. However, direct data are lacking in that fS_2 measurements on mineral phases from the Merensky Reef are not available in the pressure range of 4.5 kilobars. However, the author's measurements of fO_2 from Merensky Reef chromites and whole rock pyroxenites indicate a range of -log fO_2 between 12.1 and 13.9 (Figures 49,50, and 51). Given this range of measured fO_2, the fS_2 need only be a minimum of - log 5.9 to develop immiscible sulfide liquids (note: - log 13.9 less 8 orders of magnitude is equal to - log 5.9). Estimates of fS_2 from the data of Nagamori and Kameda (1965) indicate that mafic magmas, such as the Bushveld, may have had a general fS_2 as high as $10^{-1\pm1.5}$ atm. at 1200°C. Therefore, the general Bushveld mafic magma even before Merensky Reef emplacement could have been approximately $10^{-1\pm1.5}$ atm. of sulfur.

Buchanan and Nolan derived the ratio of 10^8 in a magma under one atmosphere pressure. However, Sharpe et al. (1980) estimated that the Merensky Reef crystallized under a pressure of 4.5 kilobars. Therefore, a pressure correction should be applied to the measured intrinsic oxygen fugacity, performed at one atmosphere, to determine if the 10^8 ratio is still exceeded when the pressure correction is integrated. Assuming that sulfur was at a constant fS_2 value of $10^{-1} \pm 1.5$ and further assuming that the intrinsic oxygen fugacity was mostly or completely buffered by carbonaceous fluids, the author could apply a pressure correction for the fO_2 values, utilizing data from Sato and Valenza (1980), Figure 54. The

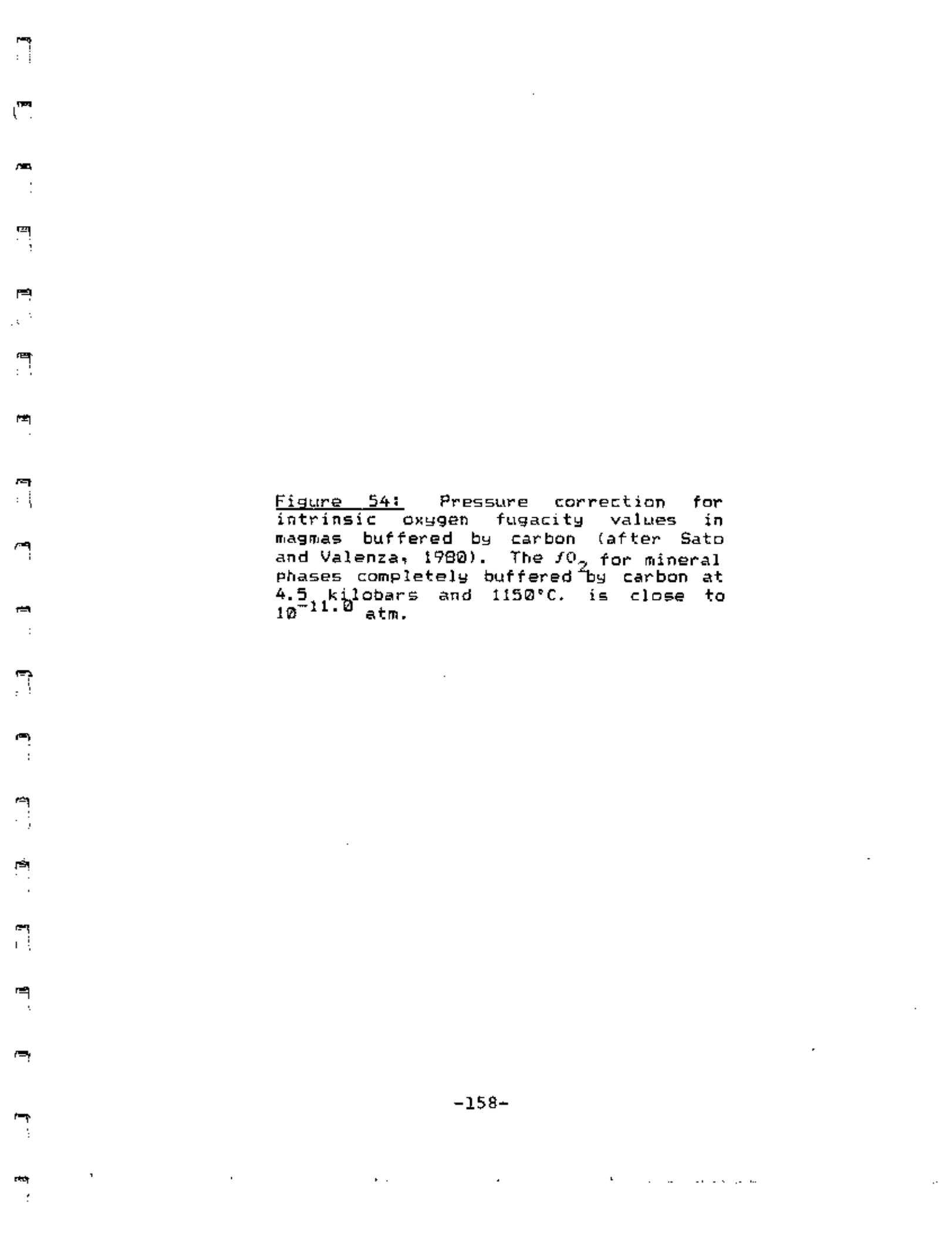

Figure 54: Pressure correction for intrinsic oxygen fugacity values in magmas buffered by carbon (after Sato and Valenza, 1980). The fO_2 for mineral phases completely buffered by carbon at 4.5 kilobars and 1150°C. is close to $10^{-11.0}$ atm.

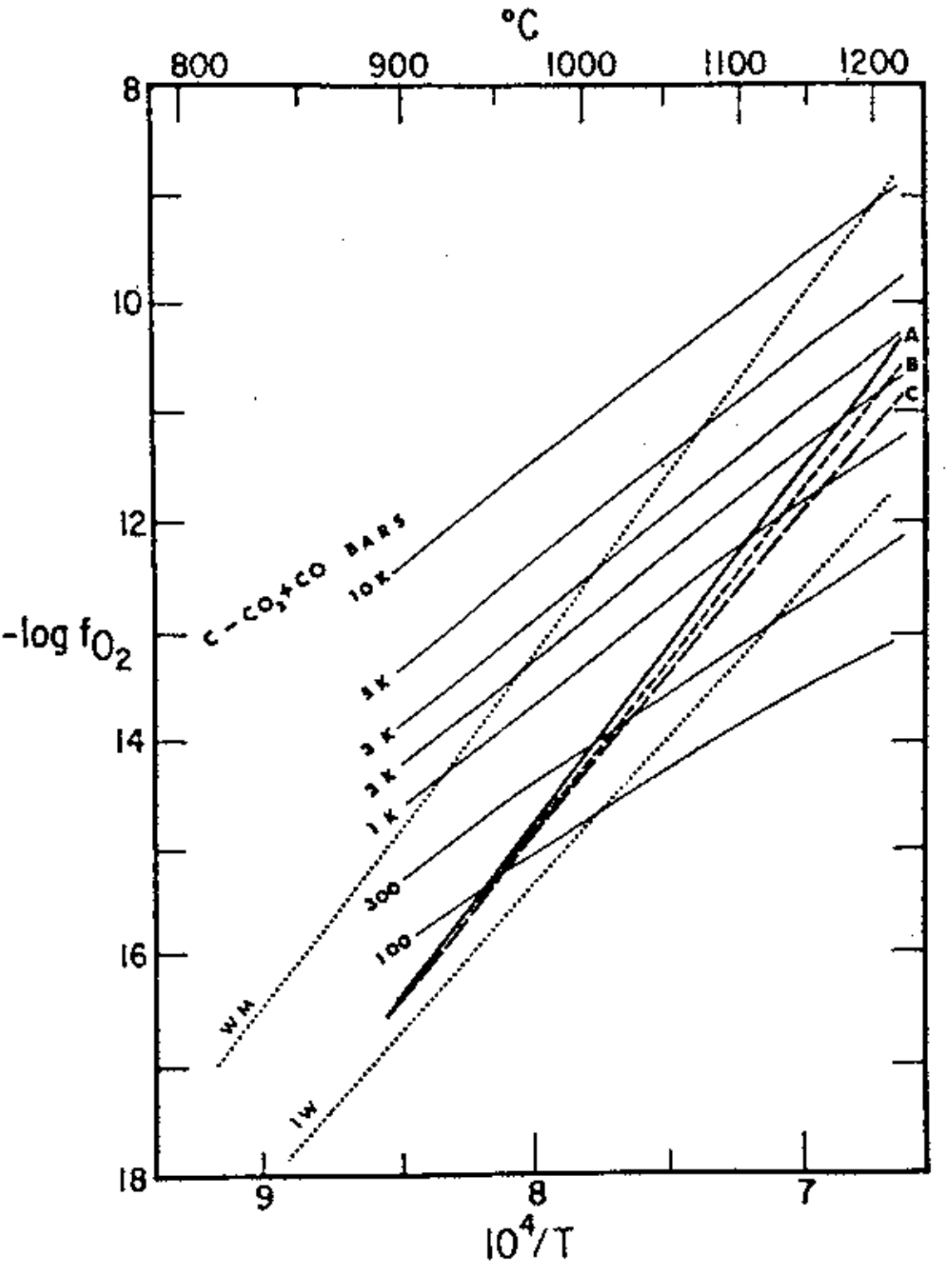
°C
800
900
1000
1100
1200
8
10
12
14
16
18
-log f_{O_2}
C - CO_2 - CO
BARS
10K
5K
3K
2K
1K
300
100
WM
IW
A
B
C
9
8
7
$10^4/T$

diagram indicates any magma buffered by C-(CO-CO_2) at 1150°C and at 4.5 kilobars pressure would have a log fO_2 of approximately 10^{-11}. Utilizing this pressure corrected value for the fO_2 of carbon buffered systems, the fS_2/fO_2 value needed for immiscibility, 10^8, would only require a minimum of 10^{-3} fS_2. Consequently, the author's carbon buffered and pressure corrected log fO_2 value of 10^{-11} at 1200°C. and the referenced log fS_2 value of $10^{-1\pm1.5}$ at 1200°C. exceeds the required ratio of 10^8 for the development of sulfide immiscibility (calculations for the ratio of fS_2/fO_2 as determined by this author for the Merensky Reef are shown in Appendix V). If the assumption of carbon buffering is not used, less of a pressure correction is needed, i.e., the fO_2 may be more reduced and closer to the 10^{-12} to 10^{-14} value range measured in this work. This is true because most silicate redox equilibria are not as pressure dependent as are the carbon-carbon dioxide equilibria; this has been previously discussed by Ulmer (1978). If indeed the fO_2 are more reduced, then even less of an increase in fS_2 is needed to reach the immiscibility ratio of 10^8.

Mass balance calculations cited in our publication (Elliott et al., 1982) provide an estimate of the thickness of magma needed to be "scrubbed" by the developing immiscible sulfide in order to attain its present enrichment in platinum group elements. Our calculation of only a few hundreds of meters of magma being needed is interesting in that the dissemination of carbonaceous fluids (lowering the fO_2 and

producing sulfide liquid) throughout the magma chamber is easily envisioned via a plutonic fumarole adding fluids which quickly "communicate" with this amount of magma within the chamber. On the other hand, the hypothesis of sulfides arising from an injection of hot, new magma is difficult to imagine in that said magma would have to spread evenly (approximately one meter) and quickly over the entire Bushveld chamber floor (hundreds of meters in dimension). Additionally, the hypothesis of sulfide development in a fractionating magma in situ in a closed system is refuted by the work of Liebenberg (1970) in that the sulfide concentration within the Merensky Reef is two orders of magnitude greater than in both the hanging wall and footwall; Liebenberg (1970) also favored the distillation of carbon, sulfur, and arsenic from footwall sediments into the Bushveld chamber.

In summary, the author concludes that the plutonic fumarole hypothesis not only accounts for the development of geochemical gradients from potholes to the Normal Merensky Reef but also that the hypothesis could provide for a genetic relationship between plutonic fumaroles and the chamber wide precipitation of the Merensky Reef.

The Origin of Carbon in the Bushveld Complex

Understanding the nature and origin of carbon is tantamount to testing the plutonic fumarole hypothesis in that the hypothesis assumes that carbon controls the fO_2 of the Bushveld magma. The carbon analyses shown in this study

demonstrate that much of the carbon from potholes and adjacent Normal Merensky Reef is in the form of graphite or carbides with essentially no organic carbon (see Appendix III B). The analyses further showed that inorganic carbon exists in the footwall of the Merensky Reef.

The plutonic fumarole hypothesis can readily account for high levels of carbonaceous compounds in the Merensky Reef but it is doubtful that the hypothesis could account for inorganic carbon in 687 meters of footwall (as previously discussed and also implied by the low values shown in Figure 52). The author postulates that the inorganic carbon in the footwall may be a "background" value intrinsic to the magma from its upper mantle origin whereas the higher carbon values in the Merensky Reef proper are derived from a metasomatic origin. Sato and Valenza (1980) discussed with reference to the Skaergaard intrusion that graphite may be present and brought up from the upper mantle as a stable compound. Therefore, any new injection, such as that inferred by Cameron at the L-horizon, for magma brought into the Bushveld chamber from the upper mantle could also contain graphite.

In summary, two distinct sources of Bushveld carbon are possible: 1) inorganic carbon from the upper mantle which could have contributed to the consistently reduced condition of the Critical Zone as shown by Elliott et al. (1982), and 2) organic carbon baking out of the sedimentary floor rocks in the form of carbonaceous fluids which "cracked" upon reaching the magmatic temperatures, producing graphite

enrichment in potholes and concomitant enrichment on the adjacent Normal Merensky Reef.

The ultimate proof of the plutonic fumarole hypothesis may depend on stable carbon isotopic studies, although as just discussed the pothole graphite may be derived both by the "cracking" of carbonaceous volatile fluids and /or by emaniations from mantle regions.

CONCLUSIONS

1) Lateral gradients of O, C, total Fe, Mg, Al, and Cr exist from potholes to adjacent Normal Merensky Reef.

2) Vertical gradients of O and C exist between the Merensky Reef and its footwall.

3) The Rustenburg Pothole bottom show greater reduction ($10^{-13.4}$) than the pothole edge ($10^{-13.2}$) which in turn shown greater reduction than the adjacent Normal Merensky Reef ($10^{-12.9}$).

4) The concentration of inorganic carbon is far greater in Merensky Reef potholes (approximately 1,800 ppm) than in the Merensky Reef footwall (approximately 200 ppm).

5) Complete or partial buffering of fO_2 by equilibria in a carbonaceous-rich system such as C-(CO-CO_2) may have occured at least locally in the Bushveld magma.

6) Immiscible sulfide development in the Bushveld magma was possibly triggered by exceeding the fS_2/fO_2 miscibility ratio by the injection of carbonaceous and/or sulfurous gases via plutonic fumaroles.

7) The plutonic fumarole hypothesis developed by Ulmer (1981) not only accounts for the geochemical gradients measured in this study but also may account for the petrogenesis of the Merensky Reef proper.

8) Hypotheses which envision potholes as resulting from convective scouring are clearly refuted, and while Von Gruenewaldt's hypothesis may be valid it can not account in

its present form for the simultaneous development of the geochemical gradients found in this study, particularly the carbon.

Even though these conclusions are based on only three of an enormous population of potholes, they do form a coherent data set. Obviously, this is/was a pilot study and will need to be enlarged by future research to confirm/refute the plutonic fumarole hypothesis.

BIBLIOGRAPHY

Albee, A.L., and Ray, L., 1970, Correction factors for electron probe microanalysis of silicates, oxides, carbonates, phosphates, and sulphates: Anal. Chem., 42, 1408-1414.

Bence, A.E., and Albee, A.L., 1968, Empirical corrections factors for the electron microanalysis of silicates and oxides: Jour. Geology, 76, 382-403.

Buchanan, D.L., and Nolan, J., 1979, Solubility of sulfur and sulfide immiscibility in synthetic tholeiitic melts and their relavance to Bushveld Complex rocks: Can. Mineralogist, 17, 483-494.

Cameron, E.N. and Desbourough, G.A., 1969, The occurence and characteristics of chromite deposits--eastern Bushveld Complex: Econ. Geol. Mono. 4, 23-40.

Cameron, E.N., 1970, Compositions of certain coexisting phases in the eastern part of the Bushveld Complex: Geol. Soc. of S. Africa, Spec. Pub. 1, 1970: Symposium on the Bushveld Igneous Complex and Other Related Igneous Intrusions, 46-58.

Cameron, E.N., 1982, The upper critical zone of the eastern Bushveld Complex--precursor of the Merensky Reef: Econ. Geol., 77, 1307-1327.

Collins, H.B., Eggler, D.H., Eminhizer, L., 1975, Manual of operating procedures for the ETEC "Autoprobe": Mineral Constitution Laboratory, Penn State University, 29 pp.

Darken, L.S., and Gurry, R.W., 1945, The system iron-oxygen. I. The wustite field and related equililbria: J. Amer. Chem., 67, 1398-1412.

Deines, P., Nafziger, R.H., Ulmer, G.C., and Woermann, E., 1974, Temperature-oxygen fugacity tables for selected gas mixtures in the system C-H-O at one atmosphere total pressure: Pennsylvania State Univ., Earth Mineral Sci. Expt. Sta. Bull., # 88, 129 pp.

Elliott, W.C., 1981, Petrogenetic study of a platiniferous zone of the Stillwater Complex, Montana: Unpublished M.A. dissertation, Temple University, 146 pp.

Elliott, W.C., Grandstaff, D.E., Ulmer, G.C., Buntin, T.J., 1982, An intrinsic oxygen fugacity study of Platinum-Carbon association in layered intrusions: Econ. Geol., 77, 1493-1510.

Eugster, H.P., and Wones, D.R., 1962, Stability relations of the ferruginous biotite, annite: Jour. Petrology, 3, 82-125.

Ferguson, J., and Botha, E., 1963,Some aspects of igneous layering in the basic zones of the Bushveld Complex: Geol. Soc. South Africa Trans., 66, 259-282.

Finger, L.W., and Hadidiacos, C.G., 1971, Aspects of computer automation of an electron microprobe: Carnegie Institution Year Book 70, # 16, 269-275.

Flynn, R.T., Ulmer, G.C., and Sutphen, C.F., 1978, Petrogenesis of the Eastern Bushveld Complex: Crystalization of the Middle Critical Zone. J. Petrology, 19, 136-152.

French, B.M., and Eugster, H.P., 1965, J. Geophys. Res., 70, 1529-1539.

Haughton, D.R., Roeder, P.L., and Skinner, B.J., 1974, Solubility of sulfur in mafic magmas: Econ. Geol., 69, 451-467.

Huebner, J.S., 1971, Buffering techniques for hydrostatic system at elevated pressures, in Ulmer, G.C., ed., Research techniques for high pressure and high temperature: New York, Springer-Verlag, 123-179.

Hutchinson, C.S., 1974, Laboratory handbook of petrographic techniques: John Wiley and Sons, New York, 527pp.

Liebenberg, L., 1970, The sulfides in the layered sequences of the Bushveld Igneous Complex: Geol. Soc. South Africa, Spec. Pub. 1, 108-207.

Muan, A., 1955, Phase equilibria in the system $FeO-Fe_2O_3-SiO_2$: J. Metals, 1, Trans. Metal. Soc., AIME, 203, 965-976.

Muan, A., and Osborn, E.F., 1956, Phase equilibria at liquidus temperatures in the system $MgO-FeO-Fe_2O_3-SiO_2$: Am. Soc. Jour., 39, 121-140.

Nafziger, R.H., Ulmer, G.C., and Woermann, E., 1971, Gaseous buffering for the control of oxygen fugacity at one atmosphere, in: Ulmer, G.C., ed., Research Techniques for High Pressure and High Temperture: New York, Springer-Verlag, 9-42.

Nagamori, M., and Kameda, M., 1965, Equilibria between Fe-S-O system melts and $CO-CO_2-SO_2$ gas mixturesat 1200°C: Jap. Inst. Metall. Trans., 6, 21-30.

Palladino, A.E., 1960, Phase equilibria in the ferrite region of the system FeO-MgO-Fe_2O_3: Am. Ceram. Soc. Jour., 43, 183-191.

Sato, M., 1971, Electrochemical measurements and control of oxygen fugacity and other gaseous fugacities with solid electrolyte sensors, in Ulmer, G.C., ed., Research techniques for high pressure and high temperature: New York, Springer-Verlag, 43-100.

Sato, M., 1972, Intrinsic oxygen fugacities of iron bearing oxide and silicate minerals under low total pressure: Geol. Soc. America Mem. 135, 289-307.

Sato, M., and Valenza, M., 1980, Oxygen fugacities of the layered series of the Skaergaard intrusion, East Greenland: Am. Jour. Sci., v. 280-A, 134-158.

Sharpe, M.R., Bahat, D., and Von Gruenewaldt, G., 1990, The concentric elliptical structure of feeder sites to the Bushveld complex and possible economic implications: Inst. Geol. Res. Bushveld Complex, Univ. Pretoria, Res. Rep. 24, 12pp.

Sharpe, M.R., and Snyman, J.A., 1980, A model for the emplacement of the eastern compartment of the Bushveld complex. Tectonophysics, 65, 85-110.

Speidel, D.H., and Osborn, E.F., 1967, Element distribution among coexisting phases in the system MgO-FeO-Fe_2O_3-SiO_2 as a function of temperature and oxygen fugacity: Am. Mineralogist, 52, 1139-1152.

Stevens, R.E., 1944, Composition of Some Chromites of the Western Hemisphere: Am. Mineralogist, 29, 1-34.

Ulmer, G.C., 1964, Oxidation-reduction and equilibrium phase relations at 1300°C at oxygen pressures from 0.21 to 10^{-14} atmospheres for the spinel solid solutions series $FeCr_2O_4$-$MgCr_2O_4$ and $FeAl_2O_4$-$MgAl_2O_4$: Ph.D. thesis, Pennsylvania State University, 159pp.

Ulmer, G.C., 1969, Experimental investigations of chromite spinels, in: Wilson, H.D.B., ed., Magmatic Ore Deposits, A Symposium: Econ. Geol. Monograph no. 4, 114-131.

Ulmer, G.C., 1970, "Chromite Spinels." Chapter 6 in the two volume work entitled, High Temperature Oxides edited by Dr. A Alper for the Margrave Series by Academic Press, 251-315.

Ulmer, G.C., 1978, et sequitur, Intrinsic oxygen fugacity newsletter: available on request from Geology Department, Temple University, Philadelphia, Pensylvania 19122.

Ulmer, G.C., 1980, Glimpes of Mantle Redox Conditions?, Transactions, American Geophysical Union, 61, #17, 413.

Ulmer, G.C., 1981, "Spinel Group - Rhodes Fairbridge Encyclopedia of Mineralogy", editor Keith Frye, Hutchinson Ross Publishing Company, 479-483.

Ulmer, G.C., and White, W.B., 1966, "Existence of chromous ion in the spinel solid solution series $FeCr_2O_4$." J. Amer. Ceram. Soc., 49, # 1, 50-51.

Ulmer, G.C., Woermann, E., Knecht, R, and Rosenhauser, M., 1979, "The Role of Pressure on Redox Buffers". (Invited paper, V. 70), EOS 59, #4, 398. (abstr.)

Ulmer, G.C., Elliott, W.C., Gold, D.P., 1981, Origin of Merensky platinum: Redox geochemistry or fortuitous geophysics, Platinum Symposium CSIR, Pretoria, Africa, p.52, (abstr.).

Vermaak, C.G., 1970, The geology of the lower portion of the Bushveld complex and its relationship to the floor focks in the area west of the Pilanesberg, Western Transvaal: Geol. Soc. South Africa, Spec. Pub. 1, 242-265.

Vermaak, C.F., and Von Gruenewaldt, 1981, Third International Platinum Symposium, Excursion Guidebook, Geological Society of South Africa, 62pp.

Virgo, D., and Ulmer, G.C., 1973, The Fe^{+3} site preference in the solid solution series $MgCr_2O_4$-$MgFe_2O_4$, Carnegie Institution Yearbook, 72, 567-569.

Von Gruenewaldt, G., 1979, A review of some recent concepts of the Bushveld complex with particular reference to sulfide mineralization: Can. Mineralogist, 17, 223-256.

Wasilewski, P., Virgo, D., Ulmer, G.C., and Schwerer, F.C., 1974, Magnetic properties of spinels synthesized at 1300°C in the $FeCr_2O_4$-Fe_3O_4 solid solution series: Carnegie Institution Yearbook, 73, 327-341.

Wasilewski, P., Virgo, D., Ulmer, G.C., and Schwerer, F.C., 1975, Magnetochemical characterization of $Fe(Fe_xCr_{2-x})O_4$ spinels: Geochimica et Cosmochimica Acta, 39, 889-902.

Woermann, E., Knecht, R., Rosenhauer, M., and Ulmer, G.C., 1977, "Die stabilitat des graphit im system C-O"., Fortschritte Mineralogie, 55, # 1, p. 155. (abstr.)

APPENDIX I A

Rustenburg
fO_2 - Temperature Data

Pothole Bottom Chromite (sample C)

Avg. Temp. (°C)	- log fO_2	T(°C)*	Calculated Error(±log Units)
	Up-Temperature Direction		
939	16.51	4	.06
990	15.89	3	.04
1039	15.17	3	.04
1099	14.38	1	.01
1122	13.72	2	.03
1144	13.28	1	.01
	Down-Temperature Direction		
1112	13.95	2	.03
1082	14.47	3	.04
1007	15.96	3	.04
897	17.50	5	.08
	Up-Temperatue (Rerun)		
997	16.03	3	.04
1137	13.33	1	.01

* Designates the temperature differential in °C between upper and lower cell thermocouples.

Pothole Bottom Anorthosite (Sample C)

Avg. Temp. (°C)	$-\log fO_2$	T(°C)*	Calculated Error(±log Units)
	Up-Temperature Direction		
897	16.50	2	.03
947	15.89	2	.03
996	15.30	1	.01
1045	14.53	1	.01
1094	13.92	1	.01
1153	13.06	1	.01
	Down-Temperature Direction		
1128	13.16	1	.01
1103	13.62	1	.01
1028	14.88	1	.01
978	15.46	2	.03
893	16.43	2	.03
	Up-Temperature (Rerun)		
1043	14.50	1	.01
1150	12.96	1	.01

* Designates the temperature differential in °C between upper and lower cell thermocouples.

Pothole Bottom Pegmatoidal Pyroxenite (Sample C)

Avg. Temp. (°C)	$-\log fO_2$	T(°C)*	Calculated Error(±log Units)
	Up-Temperature Direction		
849	17.77	1	.01
889	17.13	5	.08
987	15.74	5	.08
1041	14.98	2	.03
1086	14.16	3	.04
1120	13.59	4	.06
1144	13.19	1	.01
	Down-Temperature Direction		
1109	13.80	4	.06
1079	14.38	5	.08
1004	15.87	5	.08
900	17.26	2	.03
	Up-Temperature (Rerun)		
1001	15.78	2	.03
1135	13.18	3	.04

* Designates the temperature differential in °C between upper and lower cell thermocouples.

Pothole Edge Chromite (Sample B)

Avg. Temp. (°C)	$-\log fO_2$	T(°C)*	Calculated Error(±log Units)
	Up-Temperature Direction		
894	16.69	5	.08
936	16.13	6	.10
983	15.57	5	.08
1032	15.82	6	.10
1080	14.22	5	.08
1115	13.38	5	.08
1144	13.11	5	.08
	Down-Temperature Direction		
1130	13.21	4	.06
1100	13.69	4	.06
1049	14.46	4	.06
998	15.23	4	.06
882	16.84	6	.10
	Up-Temperature (Rerun)		
1010	15.04	4	.06
1130	13.22	5	.08

* Designates the temperature differential in °C between upper and lower cell thermocouples.

Pothole Edge Anorthosite (Sample B)

Avg. Temp. (°C)	- log fO_2	T(°C)*	Calculated Error(±log Units)
	Up-Temperature Direction		
900	15.31	1	.01
948	15.12	5	.08
998	14.53	5	.08
1047	14.20	5	.08
1096	13.44	5	.06
1128	13.06	5	.08
1167	12.47	6	.10
	Down-Temperature Direction		
1148	12.58	5	.08
1106	13.21	5	.08
1047	14.18	6	.10
976	15.12	5	.08
910	15.95	6	.10
	Up-Temperature (Rerun)		
1076	13.85	7	.12
1154	12.66	5	.08

* Designates the temperature differential in °C between upper and lower cell thermocouples.

Pothole Edge Pegmatoidal Pyroxenite (Sample B)

Avg. Temp. (°C)	- log fO_2	T(°C)*	Calculated Error(±log Units)
	Up-Temperature Direction		
885	15.08	6	.10
935	14.75	6	.10
983	14.26	5	.08
1030	13.84	6	.10
1079	13.37	6	.10
1109	13.27	4	.06
1146	12.63	3	.04
	Down-Temperature Direction		
1133	12.77	4	.06
1107	13.03	4	.06
1052	13.69	6	.10
966	14.87	7	.12
	Up-Temperature (Rerun)		
1011	14.47	6	.12
1127	12.98	4	.06

---

* Designates the temperature differential in °C between upper and lower cell thermocouples.

Normal Merensky Reef Chromite (Sample A)

Avg. Temp. (°C)	$-\log f O_2$	T(°C)*	Calculated Error(±log Units)
	Up-Temperature Direction		
892	15.87	1	.01
945	15.90	3	.04
992	15.60	2	.03
1042	14.80	3	.04
1091	13.98	1	.01
1127	13.33	1	.01
1150	12.87	1	.01
	Down-Temperature Direction		
1135	12.88	1	.01
1116	13.03	1	.01
1066	13.67	1	.01
1004	14.79	2	.03
879	16.99	4	.06
	Up-Temperature (Rerun)		
999	15.08	2	.03
1048	14.48	2	.03
1153	12.68	1	.01

* Designates the temperature differential in °C between upper and lower cell thermocouples.

Normal Merensky Reef Anorthosite (Sample A)

Avg. Temp. (°C)	- log fO_2	T(°C)*	Calculated Error(±log Units)
	Up-Temperature Direction		
889	16.21	6	.10
934	15.59	7	.12
982	14.98	7	.12
1029	14.29	7	.12
1080	13.56	6	.10
1109	13.13	5	.08
1142	12.57	4	.06
	Down-Temperature Direction		
1124	12.76	4	.06
1094	13.17	5	.08
1063	13.41	6	.10
994	14.63	7	.12
908	15.85	8	.14
	Up-Temperature (Rerun)		
1004	14.58	6	.10
1130	12.80	5	.08

* Designates the temperature differential in °C between upper and lower cell thermocouples.

Normal Merensky Reef Pegmatoidal Pyroxenite (Sample A)

Avg. Temp. (°C)	- log fO_2	T(°C)*	Calculated Error(±log Units)
	Up-Temperature Direction		
934	15.73	7	.12
984	14.88	7	.12
1034	14.11	6	.10
1080	13.49	6	.10
1109	13.18	5	.08
1144	12.68	4	.06
	Down-Temperature Direction		
1129	12.93	5	.08
1104	13.32	5	.08
1059	14.02	5	.08
999	14.86	7	.12
898	16.29	8	.14
	Up-Temperature (Rerun)		
1130	12.74	5	.08

* Designates the temperature differential in °C between upper and lower cell thermocouples.

Appendix I B

Union

fO_2 - Temperature Data

Pothole Edge Basal Chromite (Sample P-1)

Avg. Temp. (°C)	- log fO_2	T(°C)*	Calculated Error(±log Units)
	Up-Temperature Direction		
790	17.39	4	.06
903	16.05	4	.06
974	15.50	5	.08
1001	15.41	5	.08
1031	14.96	6	.10
1086	14.42	6	.10
1128	13.94	8	.14
1156	13.52	8	.14
	Down-Temperature Direction		
1144	13.66	8	.14
1120	14.10	8	.14
1076	14.69	7	.12
1026	15.42	5	.08
969	16.19	5	.08
	Up-Temperature (Rerun)		
1154	13.43	8	.14

* Designates the temperature differential in °C between upper and lower cell thermocouples.

Pothole Edge Anorthositic Footwall (Sample P-1)

Avg. Temp. (°C)	- log fO_2	T(°C)*	Calculated Error(±log Units)
	Up-Temperature Direction		
900	15.56	2	.03
969	15.07	3	.04
1029	14.50	5	.08
1082	13.99	4	.06
1125	13.54	6	.10
1149	13.26	3	.04
	Down-Temperature Direction		
1139	13.37	3	.04
1081	14.07	6	.10
1025	14.75	5	.08
964	15.46	5	.08
	Up-Temperature (Rerun)		
1055	14.37	4	.06
1154	13.14	2	.03

* Designates the temperature differential in °C between upper and lower cell thermocouples.

Pothole Edge Upper Chromite (Sample P-4)

Avg. Temp. (°C)	$-\log f O_2$	T(°C)*	Calculated Error($\pm$log Units)
	Up-Temperature Direction		
909	15.89	3	.04
1077	13.84	4	.06
1122	13.40	5	.08
1157	13.04	6	.10
	Down-Temperature Direction		
1135	13.57	6	.10
1051	14.87	5	.08
1018	15.29	4	.06
902	17.27	3	.04
	Up-Temperature (Rerun)		
1016	15.51	3	.04
1124	13.85	5	.08
1158	13.36	6	.10

* Designates the temperature differential in °C between upper and lower cell thermocouples.

Appendix I C

Impala

fO_2 - Temperature Data

Pothole Bottom Chromite (Sample P-6)

Avg. Temp. (°C)	- log fO_2	T(°C)*	Calculated Error(±log Units)
	Up-Temperature Direction		
901	17.19	1	.01
1017	15.60	0	.00
1074	14.79	0	.00
1120	14.10	0	.00
1157	13.56	2	.03
	Down-Temperature Direction		
1119	14.25	1	.01
1073	14.99	1	.01
1027	15.82	0	.00
898	17.98	2	.03
	Up-Temperature (Rerun)		
909	17.42	1	.01
1028	15.66	1	.01
1137	14.28	2	.03

* Designates the temperature differential in °C between upper and lower cell thermocouples.

Fothole Bottom Anorthosite (Sample P-6)

Avg. Temp. (°C)	$-\log f O_2$	T(°C)*	Calculated Error($\pm$log Units)
	Up-Temperature Direction		
908	17.14	2	.03
998	15.80	2	.03
1090	14.55	2	.03
1156	13.61	1	.01
	Down-Temperature Direction		
1119	14.12	2	.03
1040	15.20	2	.03
960	16.36	2	.03

Note: electrode broke, run terminated

---

* Designates the temperature differential in °C between upper and lower cell thermocouples.

Normal Merensky Reef Basal Chromite (Sample N-1)

Avg. Temp. (°C)	- log fO_2	T(°C)*	Calculated Error(±log Units)
	Up-Temperature Direction		
873	16.90	6	.10
919	16.25	7	.12
968	15.38	7	.12
1015	14.55	9	.15
1063	13.65	8	.14
1110	12.86	9	.15
1150	12.31	9	.15
1171	12.00	9	.15
	Down-Temperature Direction		
1139	12.36	9	.15
1109	12.85	8	.14
1062	13.78	8	.14
1013	14.32	8	.14
963	15.19	7	.12
865	16.99	7	.12
	Up-Temperature (Rerun)		
1003	14.51	8	.14
1100	13.00	8	.14
1151	12.30	8	.14

* Designates the temperature differential in °C between upper and lower cell thermocouples.

Normal Merensky Reef Anorthositic Footwall (Sample N-1)

Avg. Temp. (°C)	$-\log fO_2$	T(°C)*	Calculated Error(±log Units)
	Up-Temperature Direction		
887	15.36	1	.01
964	14.54	1	.01
1018	13.77	1	.01
1068	13.09	1	.01
1116	12.50	2	.03
1156	12.07	2	.03
	Down-Temperature Direction		
1138	11.96	2	.03
1101	12.32	2	.03
1057	12.84	1	.01
1007	13.43	1	.01
918	14.96	1	.01
	Up-Temperature (Rerun)		
1018	13.85	1	.01

* Designates the temperature differential in °C between upper and lower cell thermocouples.

Appendix II A

RUSTENBURG POTHOLE

Least Squares Regression Analyses of fO_2 - Temperature Data*

Stratigraphic Location	Least Squares Fit Equation**	No. of Data Points	Reg. Coef.
Pothole Bottom Chromite (fig. 30)	Y = -2.86X + 6.69	12	0.99
Pothole Bottom An Footwall (fig. 29)	Y = -2.33X + 3.26	13	0.99
Pothole Bottom Pegmatoidal Pyroxenite (fig. 31)	Y = -2.54X + 4.46	11	0.98
Pothole Edge Chromite (33)	Y = -2.39X + 3.59	14	0.99
Pothole Edge An Footwall (fig. 32)	Y = -2.31X + 3.55	12	0.99
Pothole Edge Pegmatoidal Pyroxenite (fig. 34)	Y = -2.20X + 2.82	10	0.99
Normal Merensky Chromite (fig. 36)	Y = -2.68X + 5.98	14	0.98
Normal Merensky An Footwall (fig. 35)	Y = -2.36X + 3.96	14	0.99
Normal Merensky Pegmatoidal Pyroxenite (fig. 37)	Y = -2.49X + 4.75	12	0.99

* Temperature Data Range Approximately 900°C - 1150°C.

** $Y = -\log fO_2$, $X = 10^4/T°K$

Appendix II B

UNION POTHOLE

Least Squares Regression Analyses of fO_2 - Temperature Data*

Stratigraphic Location	Least Squares Fit Equation**	No. of Data Points	Reg. Coef.
Pothole Edge Basal Chromite (fig. 39)	Y = -2.46X + 3.79	11	0.99
Pothole Edge An Footwall (fig. 40)	Y = -1.71X - 1.29	12	0.98
Pothole Edge Upper Chromite (fig. 41)	Y = -2.75X + 6.11	10	0.98

* Temperature Data Range Approximately 900°C - 1150°C.

** $Y = -\log fO_2$, $X = 10^4/T°K$

Appendix II C

IMPALA POTHOLE

Least Squares Regression Analyses of fO_2-Temperature Data*

Stratigraphic Location	Least Squares Fit Equation**	No. of Data Points	Reg. Coef.
Pothole Bottom Chromite (fig. 43)	Y = -2.41X + 3.05	12	0.97
Pothole Bottom An Footwall (fig. 44)	Y = -2.37X + 2.93	7	0.99
Normal Merensky Chromite (fig. 45)	Y = -2.74X + 7.16	17	0.99
Normal Merensky An Footwall (fig. 46)	Y = -2.21X + 3.61	12	0.98

* Temperature Data Range Approximately 900°C - 1150°C.

** $Y = -\log fO_2$, $X = 10^4/T°K$

Appendix III A

Carbon Calibration

Sample I.D.	Material	Sample Weight (grams)	Carbon (ppm)
S-1	Al_2O_3	.1278	141
		.1041	144
S-2	Al_2O_3 spiked	.1100	327
	with 200 ppm	.1016	344
	of Graphite	.1028	302

Appendix III B

Rustenburg Carbon Analyses

Sample I.D.	Sample Weight (grams)	Total Carbon (ppm)	Sample Weight (grams)	Organic Carbon (ppm)
Sample C (An)	0.495	435	0.529	59
	0.250	431	0.508	91
Sample C (pyx)	0.499	1920	0.506	199
	0.251	1950	0.519	101
Sample B (Cr)	0.506	189	0.508	41
	0.503	206	0.511	39
Sample B (An)	0.500	198	0.503	12
	0.499	203	0.515	15
Sample B (pyx)	0.506	298	0.529	43
	0.504	291	0.530	34
Sample A (Cr)	0.501	146	0.527	16
	0.500	161	0.504	21
Sample A (An)	0.313	88	0.530	4
	0.315	84	0.269	0
Sample A (pyx)	0.507	147	0.517	24
	0.499	162	0.519	24

Sample C is pothole Bottom
Sample B is pothole Edge
Sample A is adjacent Normal Merensky Reef

Cr is chromite
An is anorthosite
Peg is feldspathic pegmatoidal pyroxenite

Appendix IV A

Rustenburg Pothole

Electron Microprobe Analyses of Chromites

Sample Locality	Elements	Corrected Wt. % (Avg. of 7 Analyses)
Pothole Bottom (Sample C)	Al	18.46
	Mg	7.44
	Cr	43.08
	Fe(total)	26.21
	Fe(as FeO)	23.60
	Fe(as Fe_2O_3)	2.90
Pothole Edge (Sample B)	Al	14.54
	Mg	7.94
	Cr	40.72
	Fe(total)	31.08
	Fe(as FeO)	22.45
	Fe(as Fe_2O_3)	9.59
Adjacent Normal Merensky Reef (Sample A)	Al	12.32
	Mg	6.80
	Cr	38.44
	Fe(total)	35.45
	Fe(as FeO)	25.13
	Fe(as Fe_2O_3)	11.47

Locality	Total Fe(as FeO)/(MgO+Total Fe(as FeO))
Pothole Bottom	.779
Pothole Edge	.797
Adjacent Normal Merensky Reef	.839

Appendix IV B
Impala Pothole

Electron Microprobe Analyses of Chromites

Sample Locality	Elements	Corrected Wt. % (Avg. of 7 Analyses)
Pothole Bottom (Sample P-6)	Al	14.70
	Mg	8.05
	Cr	37.36
	Fe(total)	33.96
	Fe(as FeO)	26.92
	Fe(as Fe_2O_3	12.81
Adjacent Normal Merensky Reef (Sample N-1)	Al	9.97
	Mg	7.60
	Cr	36.34
	Fe(total)	37.02
	Fe(as FeO)	23.79
	Fe(as Fe_2O_3	14.62

Locality	Total Fe(as FeO)/(MgO+Total Fe(as FeO))
Pothole Bottom	.808
Adjacent Normal Merensky Reef	.830

Appendix IV C
Union Pothole

Electron Microprobe Analyses of Chromites

Sample Locality	Elements	Corrected Wt. % (Avg. of 7 Analyses)
Pothole Edge Basal Chromite (Sample P-1)	Al	14.20
	Mg	7.59
	Cr	38.81
	Fe(total)	34.04
	Fe(as FeO)	22.53
	Fe(as Fe_2O_3)	12.79
Pothole Edge Upper Chromite (Sample P-4)	Al	9.49
	Mg	6.97
	Cr	37.37
	Fe(total)	37.20
	Fe(as FeO)	24.42
	Fe(as Fe_2O_3)	14.21

Locality	Total Fe(as FeO)/(MgO+Total Fe(as FeO))
Basal Chromite	.817
Upper Chromite	.842

Appendix V

Calculation of fS_2/fO_2 Bushveld Ratio

Given: 1) Buchanan and Nolan's ratio of fS_2/fO_2 as 10^8 for the development of immiscible sulfide liquids, 2) the least reduced measured fO_2 from the author's Merensky Reef samples of $-\log fO_2$ of 12.1, and 3) the estimated fS_2 of mafic magma from Nagamori and Kameda of $-\log fS_2$ of 1 ± 1.5, we have the minimum ratio of fS_2/fO_2 in the Bushveld magma as being: $-\log fO_2$ $12.1/(-\log fS_2$ $1 \pm 1.5) = \log 11.1 \pm 1.5$. Also, the maximum measured fO_2 of Merensky Reef samples is $-\log fO_2$ 13.9. Therefore, the maximum ratio in the Bushveld magma is $-\log fO_2$ $13.9/(-\log fS_2$ $1 \pm 1.5) = \log 12.9 \pm 1.5$. Since only a ratio of 10^8 is necessary for sulfide immiscibility, we have exceeded this ratio in spite of using the least reduced measured fO_2 of the Merensky Reef.

Applying Sato and Valenza's pressure corrected value for mineral phases completely buffered by carbon we have a $-\log fO_2$ value of 11 at 1150°C and 4.5 kilobars of pressure. Recalculating the ratio of fS_2/fO_2 in the Bushveld magma we have $-\log fO_2$ $11/(-\log fS_2$ $1 \pm 1.5) = \log 10 \pm 1.5$. Consequently, pressure corrected fO_2 values still provide a ratio of fS_2/fO_2 in excess of 10^8.

Note: If the author's runs had been completely buffered by carbon then all fO_2 values would have been identical at a given temperature. That is, the fO_2 would have been identical to the $C\text{-}CO\text{-}CO_2$ buffer. However, in order to apply the pressure correction of Sato and Valenza the author had to

assume complete buffering. Additionally, no pressure correction exists for fS_2 at 4.5 kilobars and 1150°C. Therefore, the author's pressure corrected calculation is incomplete, but no data-set currently available rule out the fS_2/fO_2 ratio as an immiscibility trigger for the Merensky Reef.

Appendix VI

Analytical Technique

The oxygen fugacity sensor is essentially an oxygen concentration cell which is composed of two solid electrolytes (specific for O^{2-} ions): an air reference electrode (known cell), and an electrode for unknown oxygen fugacity (sample cell).

The solid electrolyte, specific to O^{2-} ions, should meet the following requirements (Sato, 1971): 1) O^{2-} ion conductivity predominates over a wide range of oxygen fugacity, 2) ionic conductivity large enough to obtain reliable electromotive force (emf) measurements over a significant temperature range, 3) the reversible electrode reaction for the ionization of molecular oxygen can take place easily at the electrolyte-conductor interface, 4) the electrolyte is thermally stable and chemically inert at desired temperatures, 5) low permeability for uncharged gas species, including molecular oxygen.

The historic solid electrolyte which met the aforementioned prerequisites was a solid solution of ZrO_2-CaO (Kiukola and Wagner, 1957). However, Dr. Sato and this author prefer a solid solution of 92 mole % ZrO_2 with 8 mole % Y_2O_3 because of its ability to: 1) function from low temperatures (700°C) to igneous temperatures (> 1300°C), and 2) minimize electronic conductivity as compared to calcia-stabilized ZrO_2.

In theory the generation of an emf across a solid electrolyte is somewhat analogous to a pH meter. In measuring hydrogen-ion concentration, the pH meter depends on the fact that solutions of different hydrogen ion concentration, located on opposite sides of a thin glass membrane, generate a potential across the membrane. The potential is dependent upon the difference in hydrogen-ion concentration. The actual pH reading is taken by utilizing a reference electrode and measuring the potential relative to the reference. In the solid electrolyte the ZrO_2-Y_2O_3 membrane is analogous to the thin glass membrane, the potential is developed by difference in O^{2-}concentration (instead of H^+), and the reference is air for the solid electrolyte cell, not a Calomel electrode as for pH meassurement.

The oxygen reference electrode has as one of its electrical connections a cap of pure Pt which is tightly secured around the outside diameter of the solid electrolyte cell. This cap of Pt fulfills prerequisite #3 of Sato's in that a potential can develop as Pt catalyzes O^{2-} ions migrating through the cell wall into O_2 molecular species by the following reaction: $2O^{2-} \xrightarrow[\text{catalyst}]{Pt} O_2 + 4e^-$. In order to complete the electronic circuit a plug of pure Pt is inserted into the reference cell until said plug is flush against the cell bottom. The chemical reaction at the plug-membrane interface is: $O_2 + 4e^- \xrightarrow[\text{catalyst}]{Pt} 2O^{2-}$. However, in laboratory useage, only the potential to perform these reactions is

measured in a very high impedance circuit so that no real migration of oxygen is allowed.

The unknown oxygen fugacity electrode consists of a capsule of $Ag_{60}Pd_{40}$ (more inert to iron-containing silicates) which is inserted into the ZrO_2-Y_2O_3 cell until the capsule is flush against the cell bottom. The "capsule electrode" thus serves a twofold purpose, i.e., sample container and electrode. Similarly as in the reference electrode, the electronic circuitry is completed by securing a cap of pure Pt around the outside diameter of the cell.

This author employed a modification of the double cell design of Sato, (1971). In our design two solid electrolyte cells are placed within a furnace of the vertical quench type as described by Muan and Osborn (1956). The cell's Pt caps are not allowed to touch as an electric short would result in addition to the possible thermal fusing of the Pt caps. The cells are manually positioned in the furnace so that they remain approximately one-half centimeter apart and are located in the furnace zone of maximum temperature, termed the "hot spot". A stream of gas composed of known ratios of CO_2 and H_2 is fed into the furnace which bridges both cells. The gas flow is regulated by a type of gas mixer designed by Darken and Gurry (1945), and modified by Muan (1955). In addition Natziger et al. (1971) provides an excellent review of gas flow regulation and calibration. The cells are allowed to equilibrate with said gas at which time the electromotive force of each cell is measured by a separate Keithley model

610c electrometer. These electrometers have an internal resistance of 10^{14} ohms (normal mode) so as to prevent any current drain in the circuitry of the cells. If a current were allowed, coulombic titration of O_2 would destroy the sample (Sato, 1971). The furnace temperature is controlled by using a Tem-Pres Research Model 32422, THERMOELECTRIC controller. However, due to temperature gradients within the furnace, thermocouples are placed adjacent to each Pt cap in order to measure the actual temperature of these cells. In addition, the melting point of the $Ag_{60}Pd_{40}$ "capsule electrode" is 1200°C. Therefore, the thermocouple is used to circumvent melting and consequent destruction of the cell.

The sample cell is sealed with SWAGELOK TEFLON compression fittings. The upper portion of the fittings has a silicon stopper through which, initially, a hypodermic needle is inserted. The $Ag_{60}Pd_{40}$ wire which connects the capsule to the electrometer is fed through the needle's capillary and then the entire cell is pump evacuated and filled with argon via the hypodermic needle. After five such argon flushings, the needle is slowly extracted thus allowing the silicon stopper to entrap argon while self-sealing around the $Ag_{60}Pd_{40}$ wire of the internal electrode. The cell is filled with high purity argon in order to remove all oxygen and other volatiles. It is true that some oxygen is found in argon as an impurity (pO_2 can not be higher than 10^{-6} atm. in the purity used). However, Palladino (1960) has stated that the oxygen species with a $pO_2 \leq 10^{-3}$ atm. in an argon/oxygen mix

is already so impoverished in oxygen species as to be very unreactive, kinetically speaking. Thus, the fO_2 of our argon is so small as to be inconsequential in comparison the the fO_2 of the unknown sample.

The reference chosen for the known or reference cell is air. The reasons being: 1) air has a constant fO_2 at sea level, with pressure correction possible, 2) air equilibrates rapidly at high temperatures, and 3) air is very inexpensive. The internal portion of the cell is constantly resupplied with air via an inexpensive diaphragm aquarium pump. Consequently, no elaborate fittings to the reference electrode are necessary because leaks are no problem, i.e., the cell is air flushed and also plumbed in ambient air.

Thermodynamics

In this study measurements of oxygen fugacity (fO_2) of condensed phases as a function of temperature were performed. As the sample is exposed to varing temperatures, a new equilibrium between the condensed phase and its vapor (oxygen in this case) will be achieved. Since the solid electrolyte is specific to O^{2-} ions, the fugacity of oxygen may be measured, because thermodynamics states that, at equilibrium in a closed system, the fugacity of oxygen in the vapor phase in association with a solid or liquid is the same as the chemical potential of oxygen in the solid or liquid. Consequently, a condensed phase may be in equilibrium with a gaseous phase even at subsolidus temperatures. In addition to

the evolution of oxygen from the condensed phase, other volatiles such as CH_4, H_2, CO, and CO_2 may be evolved. However, these emitted volatiles will also react to produce a new equilibrium condition with the emitted gaseous oxygen of the sample (for example, Sato and Valenza, 1980). Therefore, absolute intrinsic oxygen fugacity values can only be determined on samples free of volatiles other than oxygen.

Another relevant thermodynamic principle is that the electromotive force (emf) generated by the chemical potential of the oxygen gradient established across the solid electrolyte wall is proportional to the change in Gibb's Free Energy (ΔG^o). The proportionality was stated as an algebraic equality by Nernst:

$$\Delta G^o = -nFE^o \qquad (1)$$

where

n = moles of electrons (e^-)

F = Faraday constant = 96,484 Coulombs/mole e^-

E^o = millivolts

However, at equilibrium the Gibb's Free Energy, ΔG^o, may be expressed in terms of the activity quotient of a reaction, or in terms of fugacity:

$$\Delta G^o = -RT \ln f_1/f_o \qquad (2)$$

where

R = Gas Constant

T = Absolute Temperature (K^o)

f_1 = unknown fugacity (sample)

f_o = reference fugacity (known)

By combining equations one and two, an equation is derived in which the generated emf is proportional to the fugacity quotient. Thus, by measuring the generated emf from each cell through the ZrO_2-Y_2O_3 membrane, the unknown fugacity can be calculated if the reference fugacity is known. The equation is:

$$E = -RT/nF \ln f_1/f_o \quad (3)$$

Changing ln to log, and inserting numerical values for R, F, and n (being the moles of electrons transferred), we derive the equation:

$$E = -0.0496T \log f_1/f_o \quad (4)$$

Since f_o = pure O_2 gas at STP, the log f_o = log 1 = 0

and log f_1/f_o = log f_1 - log f_o

if log fO_2 =0, then log f_1/f_o = log fO_2.

Therefore, - log fO_2 = E/0.0496T(in °K). (5)

Corrections to emf Readings

As established in equation (3), the reference fugacity must be known in order to have an equation with a single unknown. Since air is used as the reference fugacity, an additional value of emf must be added to the measured emf, because air is not the usual thermodynamic standard state, i.e., it is only approximately 21% O_2. That is, equation (3) is valid only for pure O_2 at STP conditions. The correction can be calculated from the following equation:

$$E_{(air)} = (-0.0496T(\text{in } °K))(\log(0.21)) \quad (6)$$

$$= -0.033T \text{ millivolts}$$

Another correction which only involves the sample cell is termed the dissimilar metals effect. An emf is generated by the interaction between the $Ag_{60}Pd_{40}$ alloy (acting as the "capsule electrode") and the outer Pt cap electrode. Dr. Sato measured this dissimilar metals effect by employing a low-iron, nuclear-grade ZrO_2 cell. Prior studies at Temple University employing the same type of cell used by Dr. Sato did not show any marked deviation from Sato's measurement. However, figure 55 demonstrates that newer ZrO_2 cells (since 1975) have "blank corrections" that do not compare to the older values of Dr. Sato. This difference is attributed to a new type of ZrO_2 cell used by Elliott (1991) and this author. Consequently, the term "blank correction" is used instead of the Sato dissimilar metals effect to indicate that the generated emf is not only a dissimilar metals effect but also an emf error stemming apparently from microtexture and/or chemical differences in these new cells. Before 1975 cells being used in geology required no blank correction.

The new cells used in this study are low-iron, nuclear-grade ZrO_2 with 8 mole % Y_2O_3. However, an initial glassy coating, present on the outside of these cells, was found to contain an enrichment of Na, Al, and Fe. Several problems were created by this glassy coating: 1) the cell was conductive in the electronic mode, 2) vapors emitted by the glass contaminated the surrounding furnace, and 3) the glass melted at 1150°C. and said melt flowed between the Pt outer electrode cap and the ZrO_2 cell. For the interested reader,

Figure 55: Cell corrections measured in this study compared to the original dissimilar metals effect of Sato (1971) for ZrO_2 cells. The discrepancy in measurements is discussed in the text.

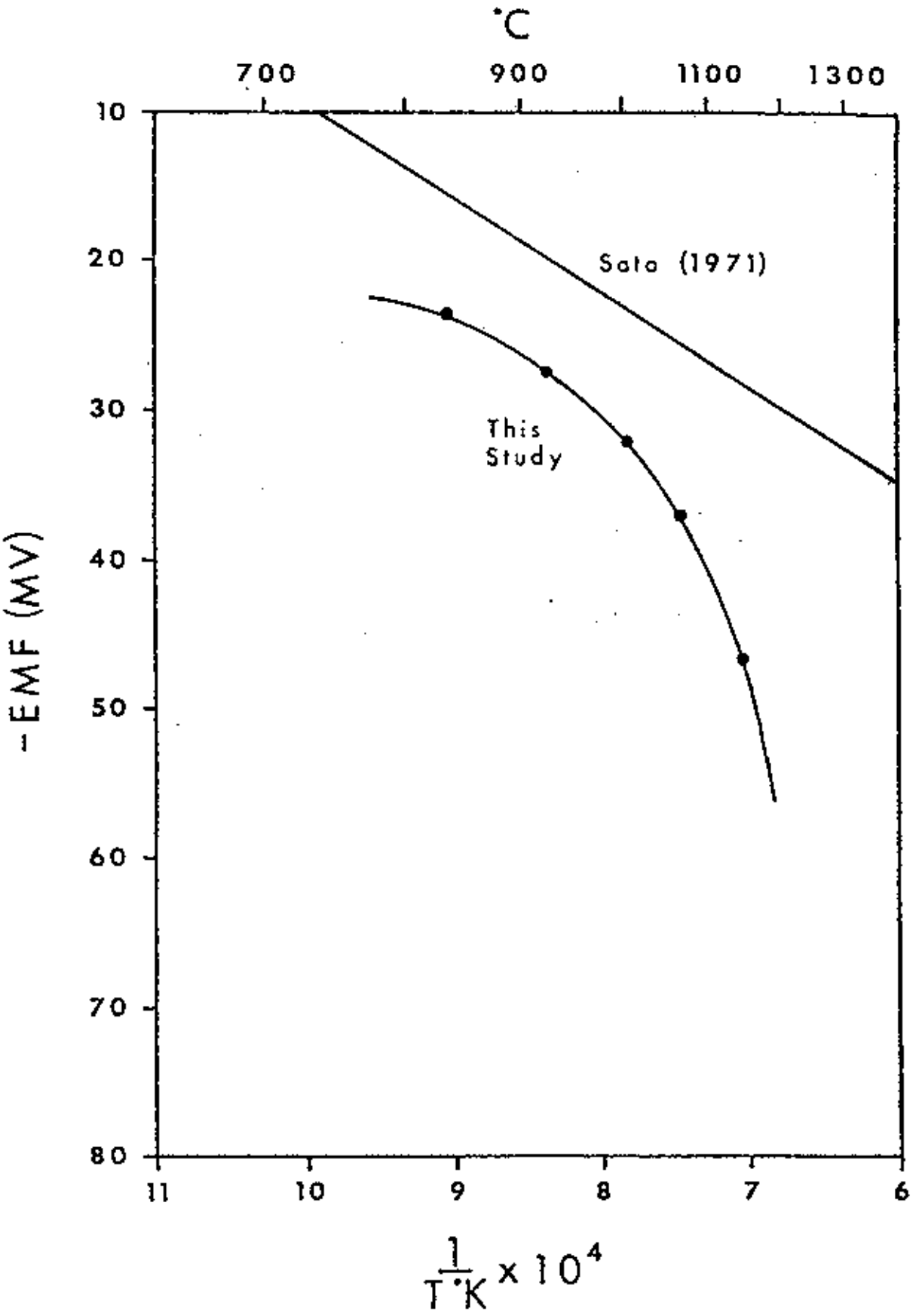
°C
700
900
1100
1300
10
20
30
40
50
60
70
80
-EMF (MV)
Sato (1971)
This Study
11
10
9
8
7
6
$\frac{1}{T°K} \times 10^4$

the above mentioned problems are addressed in detail by Elliott (1981). This glassy coating was removed by etching the cell for one to three hours, in one hour increments, in full strength reagent grade HF as needed. The actual technique and results of HF etching are given in the Intrinsic Oxygen Fugacity (IOF) Newsletter edited by Dr. Gene C. Ulmer (1978 et seq.).

Calibration of Cells

The calculation of a sample's fugacity by employing the Nernst equation (#5) requires that both cells behave in accordance with the equation. Therefore, it is imperative to periodically test the ZrO_2-Y_2O_3 cells for Nernstian behavior. The method of calibration requires the exposure of both cells to various mixing ratios of CO_2 and H_2. The mixing ratio of these gases are known and have a unique fO_2 for a particular temperature as calculated by Deines et al. (1974). The author has selected three known mixing ratios: 1) 10 parts CO_2 to 1 part H_2, termed a 10/1 mixing ratio, 2) 1 part CO_2 to 1 part H_2, termed a 1/1 mixing ratio, and 3) 1 part CO_2 to 10 parts H_2, termed a 1/10 mixing ratio.

Figure 56 demonstrates the degree of Nernstian behavior for the sample ZrO_2-Y_2O_3 cell as a function of various mixing ratios. The dashed lines are the theoretical oxygen fugacities as predicted from the Deines et al. tables; the solid lines represent solid-vapor buffer oxygen fugacities (Eugster and Wones, 1962); while the data points represent

Figure 56: Solid-vapor equilibria buffer curves and CO_2/H_2 gas mixing data for the range of temperatures employed in calibration of the ZrO_2 cells employed in this study. The QFM (quartz-fayalite-magnetite) buffer; the WM (wustite-magnetite) buffer; and the WI (wustite-iron) buffer are all from Eugster and Wones (1962). The dashed lines are CO_2/H_2 initial mixing ratios for which the fO_2-temperature data are to be found in Deines et al, (1974).

The degree of non-Nernstian behavior is shown for the sample cell as a function of mixing ratio and temperature. Ideal Nernstian behavior of the cell would be indicated by all data points plotting on the various mixing ratio lines. The sample cell data falls mostly on or slightly above the various mixing ratios. Thus, the cell's non-Nernstian behavior is oxidizing for specific temperatures and mixing ratios. Sato (1971) discusses the many variables which prevent ideal Nernstian behavior.

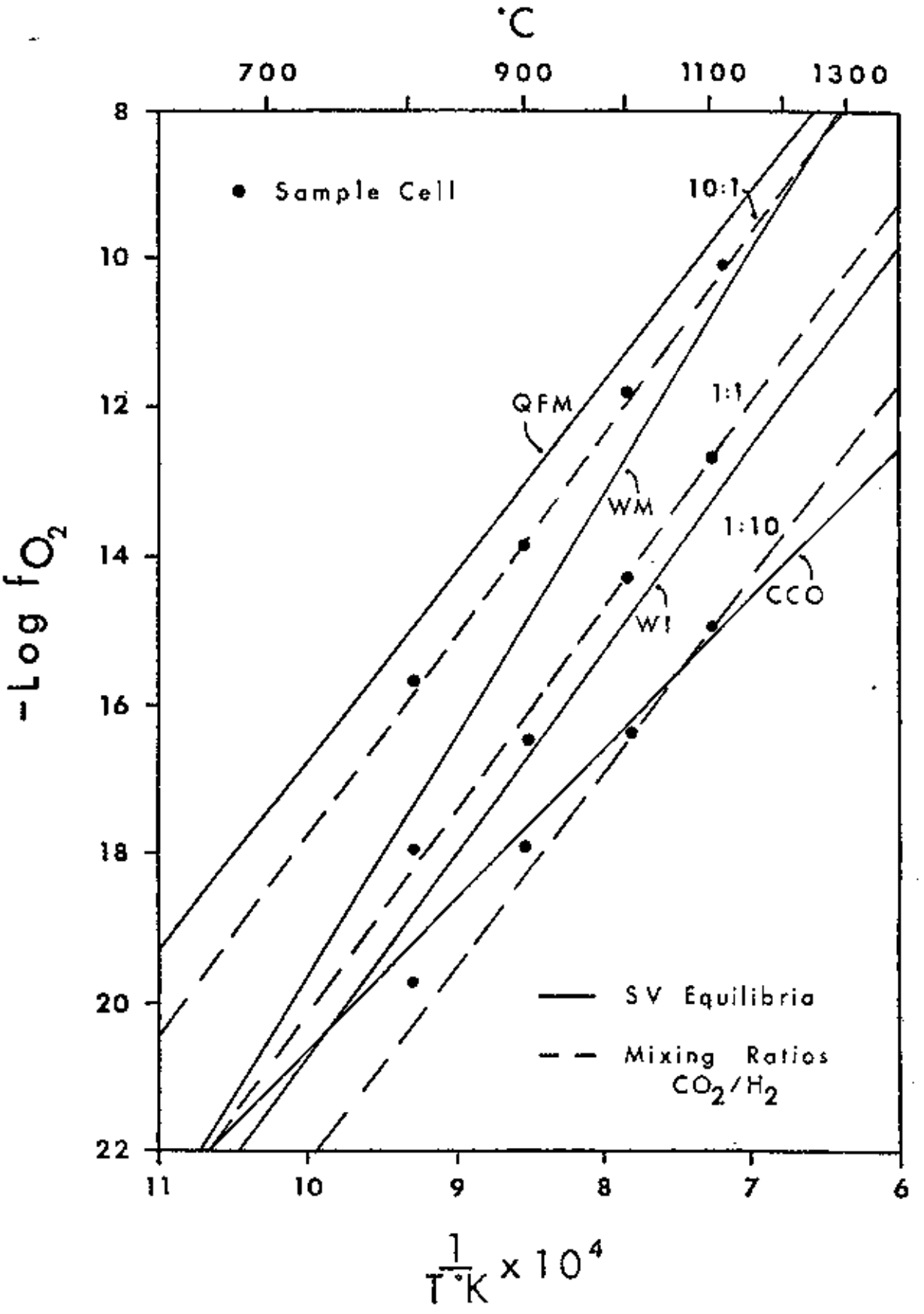
°C
700
900
1100
1300
8
10
12
14
16
18
20
22
-Log fO_2
• Sample Cell
10:1
QFM
1:1
WM
1:10
WI
CCO
SV Equilibria
Mixing Ratios
CO_2/H_2
11
10
9
8
7
6
$\frac{1}{T°K} \times 10^4$

phe measured and blank corrected fO_2 in various furnace atmospheres. The data show the standard cell is close to, but not absolutely Nernstian. Variation of a few tenth of a log unit from Nernstian behavior is usually unavoidable as discussed by Sato (1971). Additionally, non-Nernstian behavior due to a lack of gas equilibrium at low temperatures (to some small extent below 1150°C but to a seriously large extent below approximately 800°C) is discussed by Huebner (1971).

Figure 57 demonstrates the degree of Nernstian behavior for the standard (known) ZrO_2-Y_2O_3 cell as a function of various mixing ratios. All lines are analogous to those of figure 55. Similarly as with the known cell, the standard cell is close to, but not absolutely Nernstian, in that the data plot slightly below the theoretical mixing lines. Once again, non-Nernstian behavior for the standard cell is explained by Sato (1971) and Huebner (1971).

Figure 58 compares the sample and standard cells. In general, the sample cell "reads" more oxidized than the standard cell for a given temperature and mixing ratio. Also, the sample cell reads slightly more oxidized, in general, than the predicted Nernstian behavior for said ratios, while the standard cell reads slightly more reduced, in general, than the predicted Nernstian behavior for said ratios. Consequently, the sample cell will have a slightly larger positive signal due to its non-Nernatian behavior with respect to various mixing ratios while the converse applies

Figure 57: Solid-vapor and gas mixing ratio plots are discussed in figure 56. The degree of non-Nernstian behavior is shown for the standard cell as a function of mixing ratio and temperature. Ideal Nernstian behavior of the cell would be indicated by all data points plotting on the various mixing ratio lines. The standard cell is close to, but not exactly Nernstian and reads slightly reduced upon exposure to a given mixing ratio and temperature. Sato (1971) discusses the many variables which prevent ideal Nernstian behavior.

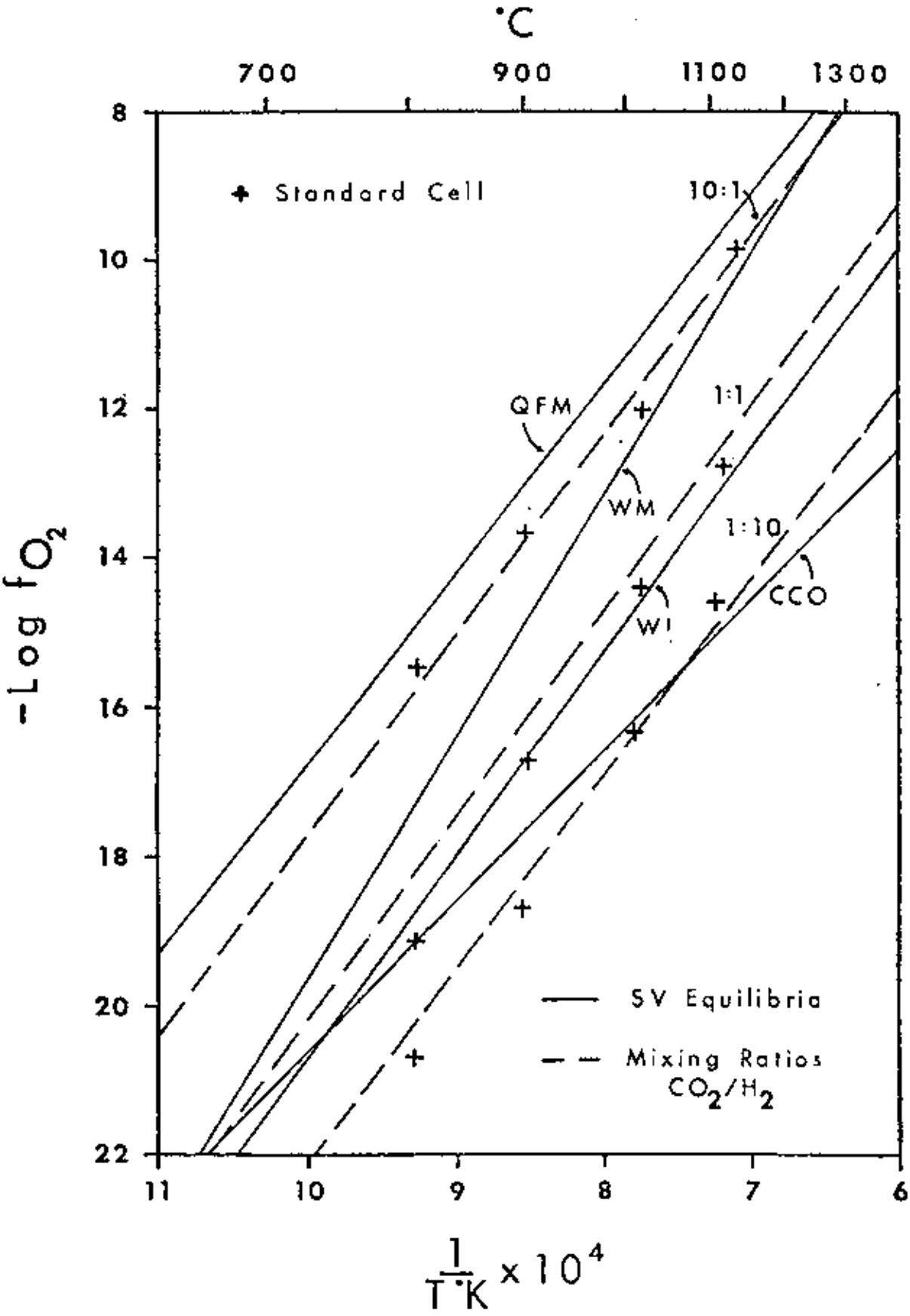
°C
700
900
1100
1300
8
10
12
14
16
18
20
22
-Log f_{O_2}
Standard Cell
10:1
QFM
1:1
WM
1:10
CCO
WI
SV Equilibria
Mixing Ratios
CO_2/H_2
11
10
9
8
7
6
$\frac{1}{T°K} \times 10^4$

Figure 58: The degree of non-Nernstian behavior is shown for the sample cell as compared to the standard cell. The sample cell, in general, reads more oxidized than the standard cell. The author employed the 1/10 mixing ratio throughout this study. The non-Nernstian behavior of the cells tend to cancel when the furnace atmosphere is a 1/10 mixing ratio as explained in the text.

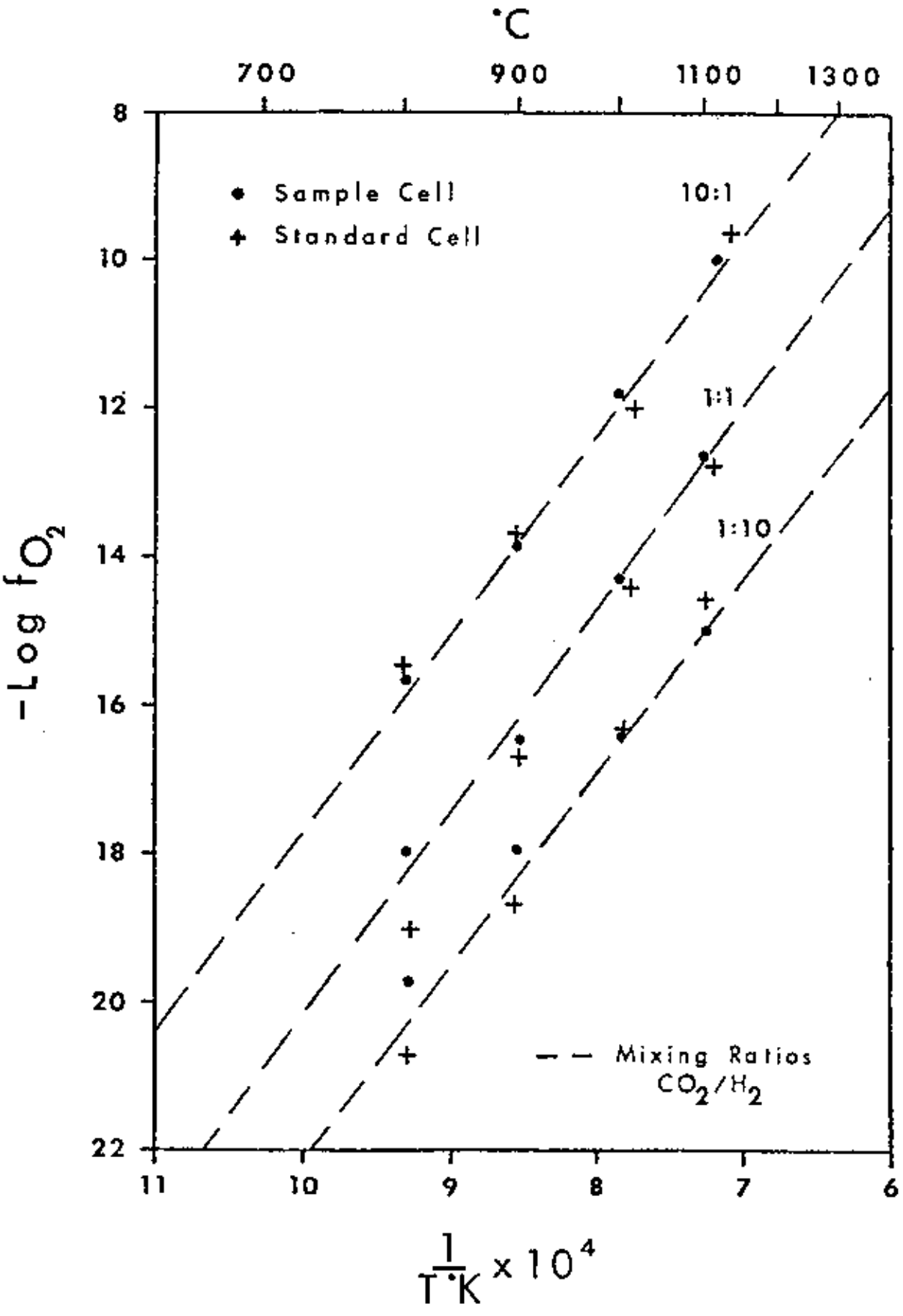
°C
700
900
1100
1300
8
10
12
14
16
18
20
22
-Log fO_2
Sample Cell
Standard Cell
10:1
1:1
1:10
Mixing Ratios
CO_2/H_2
11
10
9
8
7
6
$\frac{1}{T°K} \times 10^4$

to the standard cell. Thus, the small positive and negative non-Nernstian behavior of the sample and standard cells, respectively, tend to cancel.

In this study the author only employed the 1/10 mixing ratio for the external furnace atmosphere. This ratio was selected for the suite of samples in this study because the magnitude of the emf generated between this furnace gas and the unknown cell using the 1/10 ratio is very small, i.e., the intrinsic fO_2 of these samples is approximately that of the 1/10 mixing ratio at a given temperature. Also a small unknown cell signal is necessary to avoid Coulombic titration of oxygen into or out of the sample cell (Sato, 1971). Since the 1/1 and 10/1 ratios would produce a large emf for the suite of samples used in this study, said ratios were not used as a furnace atmosphere.

Another technique employed to determine the degree of Nernstian behavior involves useage of solid-vapor buffers (Eugster and Wones, 1962). The author selected the system wustite/magnetite (WM) with results shown in figure 59. The solid line represents the behavior of the system as determined by Eugster and Wones (1962). The data points were obtained from a 1/1 ratio of said solid buffer, total weight of 25 mg, being placed in the sample electrode bucket and exposing the cell exterior to a 1/10 mixing ratio. The data, particularly above 900°C., is in excellent agreement with the original work of Eugster and Wones (1962).

Figure 59: Calibration data for the sample cell employed in this study. The least squares fit equation (Y = -3.02X + 11.42) of the calibration data is shown as a dashed line. The calibration experiment was run against a mixture of synthetic wustite and synthetic magnetite. Since this mixture has buffering power, major leakage in the cell can still be present even with data as encouraging as this. However, the gas calibration procedures also indicate that the buffer assemblage data are accurate values.

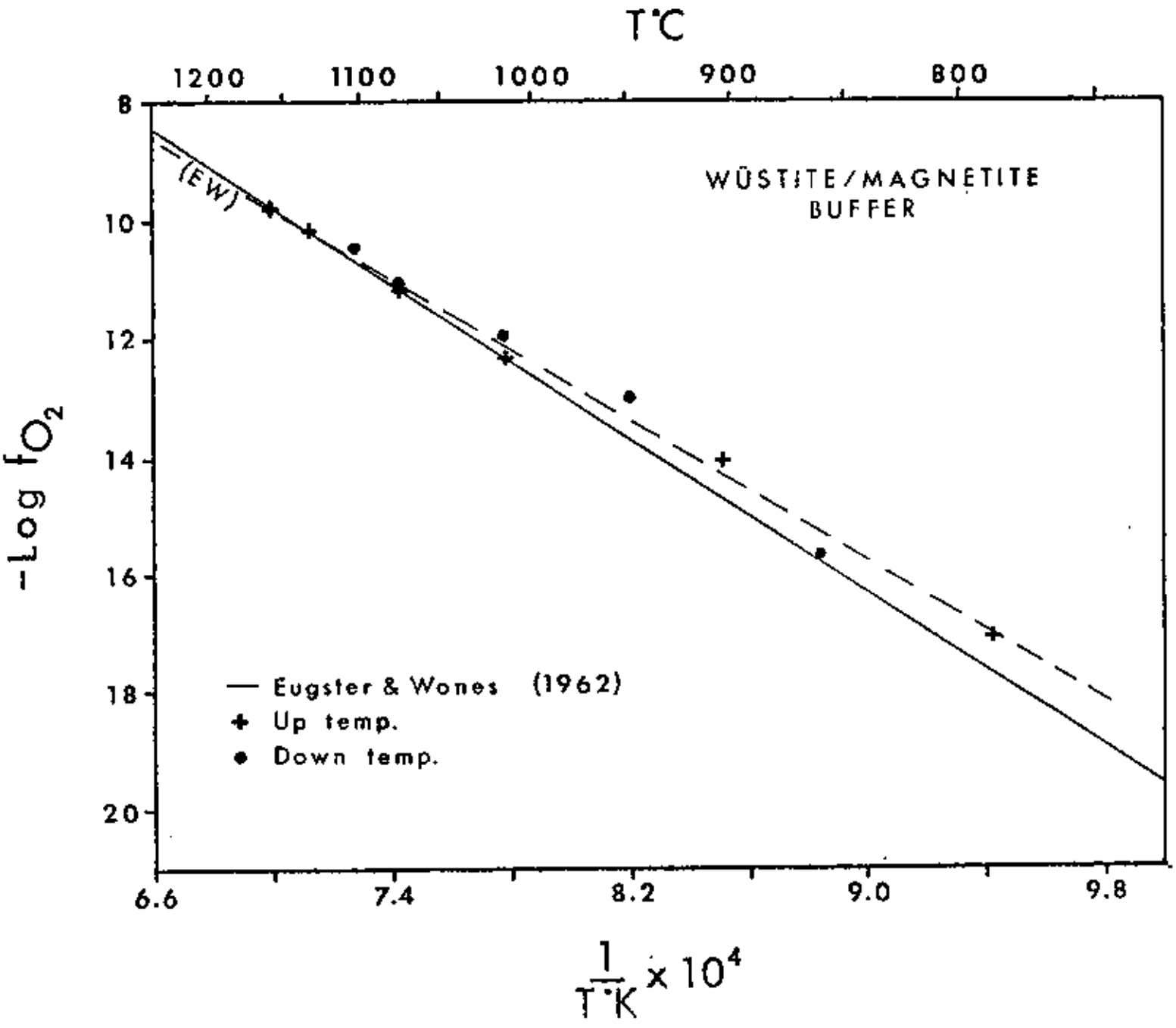
T°C
1200
1100
1000
900
800
WÜSTITE/MAGNETITE
BUFFER
(EW)
— Eugster & Wones (1962)
+ Up temp.
• Down temp.
-Log f_{O_2}
8
10
12
14
16
18
20
6.6
7.4
8.2
9.0
9.8
$\frac{1}{T°K} \times 10^4$

Figure 58 demonstrates that both cells may not exhibit totally ideal Nernstian behavior. In addition to the discussion of Sato (1971) and Huebner (1971) for non-Nernstian behavior the author tested for the possibility of non-Nernstian behavior arising from microcracks in the ZrO_2-Y_2O_3 membrane which could have expanded during heating, thus allowing the external atmosphere to physically penetrate said membrane. The author tested for the possibility of microcracks by placing pure argon in the sample cell, i.e., argon as an "unknown". Figure 60 shows that exposure of the argon filled unknown cell to various mixing ratios did not change the fO_2 of the unknown (argon) sample as a function of mixing ratio. Thus, since argon has no buffering capacity, the observed non-Nernstian behavior (figure 58 is not leakage into the ZrO_2-Y_2O_3 cell, and the measured cell blank correction (figure 55) is the only necessary correction.

Polarity of Cells

In addition to the aforementioned corrections, the polarity of the cells must be understood in order to obtain the true emf of the double cell design. In order to determine how the cells should be electronically wired, both cells are exposed to a condition in which the summation of their signals is zero. Such a condition is met by the internal and external exposure of the cells to air. The Nernst equation (#5) requires that the value of E be negative. Therefore, the cell which consistently produces the larger emf is wired to

Figure 60: In order to test for the idea of microcracks in the sample cell as a cause of non-Nernstian behavior the author used high purity argon as the "unknown sample". Symbols denote argon data for corresponding gas ratios. The fO_2 of the unknown argon sample did not vary as a function of mixing ratio as shown by the data. Since argon has no buffering capacity, any leakage of furnace atmosphere via a microcrack would change the internal fO_2 to that of the external fO_2. This clearly did not happen. Therefore, no microcracks exist and the non-Nernstian behavior is intrinsic to the cell. Note that the clustering of data points near the 1/1 mixing ratio is purely coincidential: the least squares fit shows that the data points do not plot on the 1/1 mixing ratio line.All measured argon data for corresponding gas ratios are plotted as symbols.

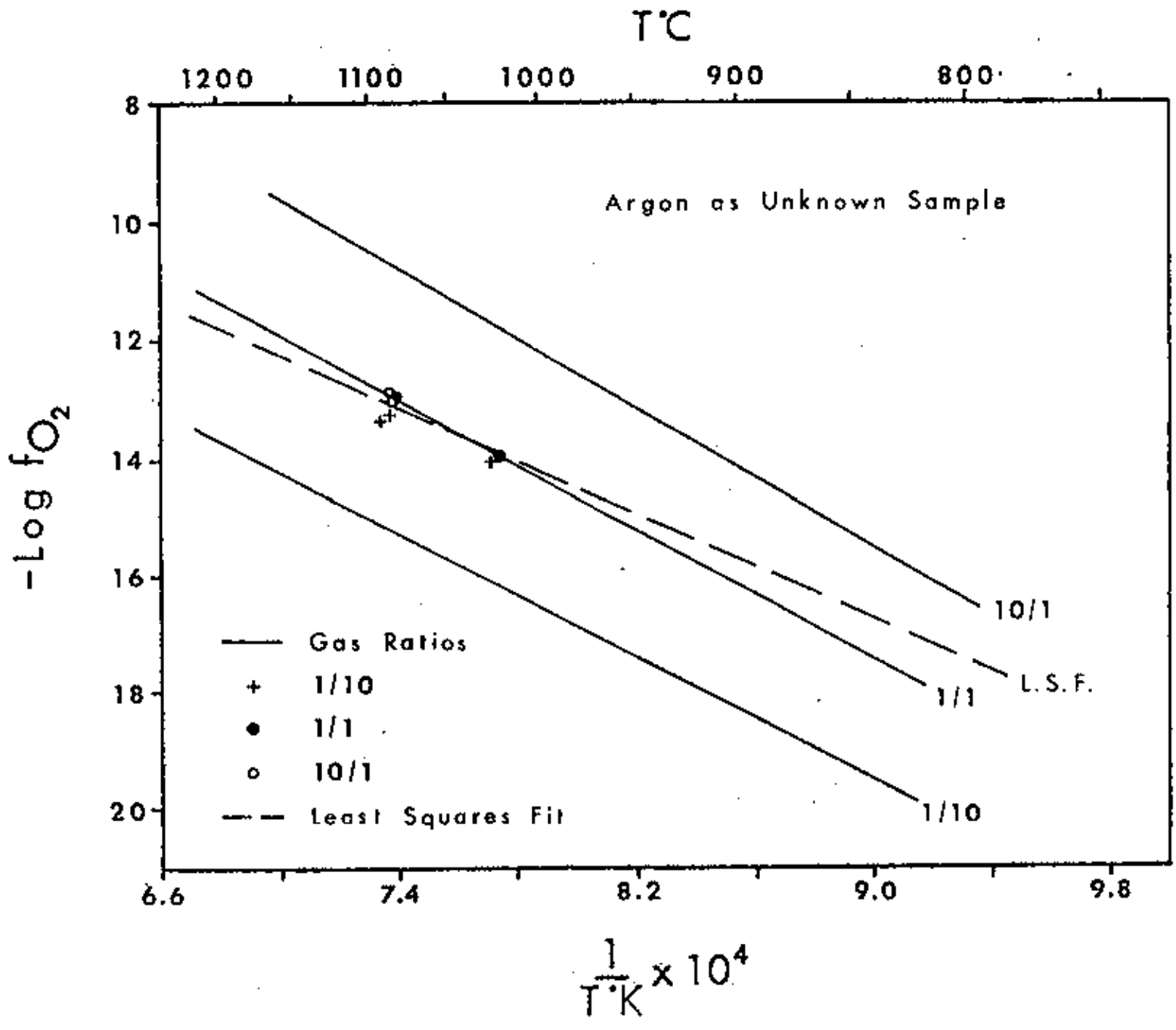
T°C
1200
1100
1000
900
800
Argon as Unknown Sample
-Log f_{O_2}
8
10
12
14
16
18
20
10/1
1/1
1/10
L.S.F.
Gas Ratios
1/10
1/1
10/1
Least Squares Fit
6.6
7.4
8.2
9.0
9.8
$\frac{1}{T°K} \times 10^4$

be electronically negative (by the sign indicator on the electrometer). In the actual readout of the emf's, the standard cell (known) versus the furnace atmosphere results in a large emf.

The standard cell has a large emf because of the extreme differences in fO_2 between air and the furnace atmosphere, whereas the sample cell has a small emf due to the furnace atmosphere being kept close in fO_2 to the fO_2 of the unknown cell by willful manual adjustment of the mixing ratios of CO_2/H_2. Since the furnace atmosphere may be more or less reducing than the unknown sample, two general polarity cases may ensue.

Polarity Case A

If the unknown cell is generating a positive signal, polarity case A is employed. A graphic discussion follows which will aid in the visualization of this case.

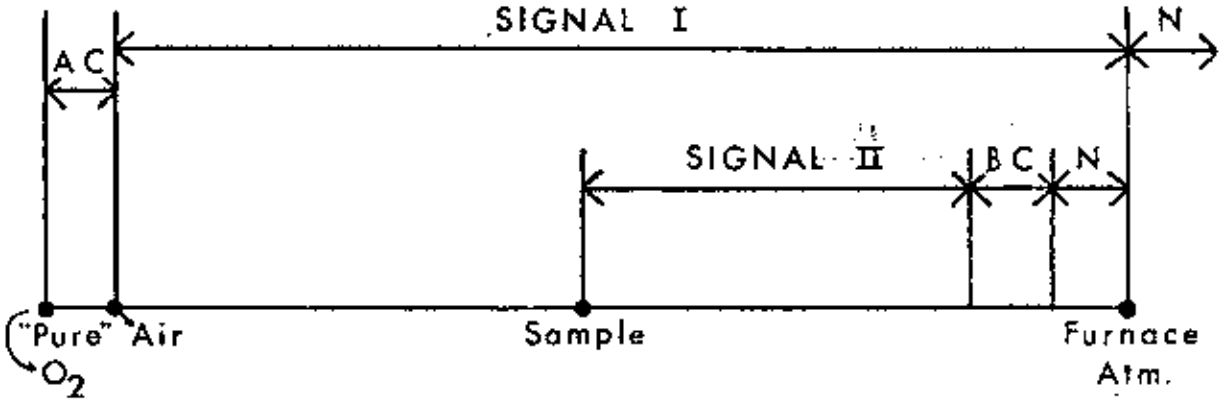

Let signal I = known cell emf which is negative

Let signal II = unknown cell emf

while

N = non-Nernstian behavior, BC = blank correction

and AC = air correction

Since the sample position and hence signal II is oxidized, relative to the furnace atmosphere, it has a positive signal. Also, the blank correction must be added to signal II since said blank correction lies between the sample and furnace atmosphere. Therefore, the true signal II emf is: (signal II)$_{(true)}$ = |actual signal II| + |blank correction| as shown diagrammatically. The magnitude of the signal between air and the sample is therefore |signal I| - |signal II$_{(true)}$|. Since the Nernst equation applies to pure O_2 gas, not air, we must add the signal between air and pure O_2. Thus, Case A is |signal I| - |signal II$_{(true)}$| +|air correction|. An important note to case A is that part of signal II arises from the fact that the unknown cell "reads" too oxidized for a 1/10 mixing ratio (figure 56), whereas the known cell "reads" too reduced for a 1/10 mixing ratio (figure 57). However, figure 58 demonstrates that the magnitude of the non-Nernstian behavior (shown diagrammatically as N) is essentially equal but opposite. Therefore, the non-Nernstian behavior essentially cancels in case A.

Special Case A

If signal II is less than the blank correction, the implication is that signal II is only negative by virture of the negative blank correction and this is a special case of case A. Therefore, signal II$_{(true)}$ = |blank correction| - |signal II|. Since signal II$_{(true)}$ is positive, this value is

substituted into case A for the final emf computation. Once again, the non-Nernstian behavior cancels in special case A.

Polarity Case B

If the sample cell is generating a negative signal which is greater than the blank correction, then polarity case B is employed. A diagrammatic discussion, employing the same nomenclature as in case A, follows:

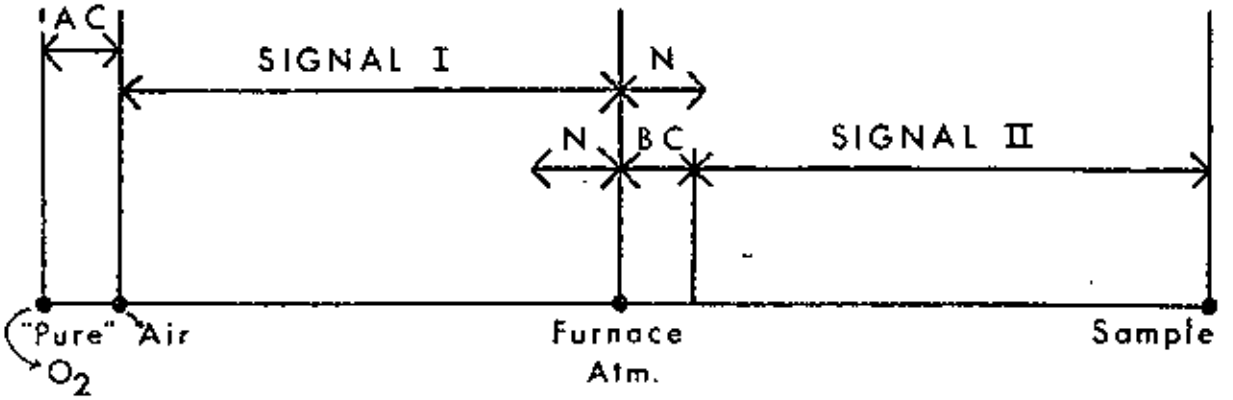

Since signal II is more reduced than the furnace atmosphere it has a negative signal. The blank correction must be substracted from signal II since it lies beyond the true intrinsic sample emf. Therefore, the true signal II emf is: |actual signal II| - |blank correction| as shown diagrammatically above. The magnitude of the signal between air and sample is: |signal I| + |signal $II_{(true)}$|. Once again, the air correction is added. Thus, polarity case B is: |signal I| + |Signal $II_{(true)}$| + air correction.

The diagram for polarity case B shows that any non-Nernstian behavior in the cells does not cancel in this case. Therefore, polarity case B must be avoided if the cells

are non-Nernstian by selecting mixing ratios that are more reducing than the sample and thereby reverting to polarity case A.

Sample Calculations

Case A

If a positive emf is generated in the unknown cell, polarity case A must be used to calculate the unknown fO_2. For example:

Given known cell emf of -900mv,

" unknown cell emf of +15mv,

" average temperature of cells being + 1100°C.

From equation # 5 we have: $fO_{2(unknown)} = emf_{(total)}/0.0496T°K$ Case A requires that the blank correction be added to the actual signal of the unknown cell. Referring to schematic case A, the blank correction for 1100°C. is found to be -44mv. Thus, the corrected unknown signal is |+15| + |-44mv| = + 59mv. The air correction from equation #6 is -0.033T°K = -0.033 * 1373°K = -45mv. The $emf_{(total)}$ for case A is |signal from known| + |corrected signal from unknown| + |air correction|. Thus, we have |-900| + |59mv| + |-45mv| = emf_{total} = + 100mv. Finally, - log $fO_{2(unknown)}$ = 100mv/(0/0496 * 1373°K) = 14.74.

Special Case A

If the unknown signal is negative but less than the blank correction we still employ Case A but with modifications. For example:

Given known emf = −10mv,

" unknown emf = −10mv,

" blank correction = −44mv,

" air correction = −45mv,

" average temperature = 1373°K,

then the corrected emf is |blank correction| − |unknown signal| = |−44| − |10| = + 34mv. Thus, emf total = |−900| + |+34| + |−45| = +979mv. Finally, $-\log fO_2$ = 979mv/(0.0496 * 1373°K) = 14.37.

Case B

Case B was not used in this study because of the non-Nernstian behavior of the cells available.